Analytical Prototypes for Ocean–Atmosphere Interaction at Midlatitudes. Part I: Coupled Feedbacks as a Sea Surface Temperature Dependent Stochastic Process*

J. DAVID NEELIN

Department of Atmospheric Sciences and Institute of Geophysics and Planetary Physics, University of California, Los Angeles, Los Angeles, California

WENJIE WENG

Department of Atmospheric Sciences, University of California, Los Angeles, Los Angeles, California

(Manuscript received 4 November 1997, in final form 14 April 1998)

ABSTRACT

Effects of ocean–atmosphere feedback processes and large-scale atmospheric stochastic forcing on the interdecadal climate variability in the North Atlantic and North Pacific Oceans are examined in a simple midlatitude ocean–atmosphere model. In the ocean, the authors consider a linearized perturbation system with quasigeostrophic shallow-water ocean dynamics and a sea surface temperature (SST) equation for a surface mixed layer. The atmosphere is represented as stochastic wind stress and heat flux forcing. This includes a noise component that depends on SST, as well as an additive component that is independent of SST. Coupling is represented by the SST dependent stochastic process, in which SST influences the probability density function of the atmospheric noise both in shifting the mean and affecting the variance. It thus includes a multiplicative noise component. The model results in both oceans indicate that large-scale additive atmospheric stochastic forcing alone (the uncoupled case) can give coherent spatial patterns in the ocean and sometimes even a weak power spectral peak at interdecadal periods. Coupling due to the SST dependent stochastic process can produce a more distinct power-spectral peak relative to the uncoupled ocean. Moreover, the time and spatial scales of the interdecadal mode are insensitive to the standard deviation of the multiplicative noise. Thus a deterministic feedback limit can be used to simplify the coupled model for further investigation of the physical mechanisms of the interdecadal mode.

In both uncoupled and coupled cases, the period of the interdecadal oscillation is determined by the zonal length scale of atmospheric wind stress and oceanic Rossby wave dynamics. The atmospheric spatial pattern sets the length scale of large-scale wave motion in the ocean. This wave propagates to the west due to oceanic Rossby wave dynamics and is dissipated at the western boundary. However, in the coupled case, the SST anomalies generated by geostrophic current can feed back to the atmosphere, which in turn brings some information back to the east and reexcites oceanic waves there. Although the magnitude of the feedback of SST on the atmosphere is much smaller than atmospheric internal variability, its effects are significant.

1. Introduction

Persistent large-scale midlatitude SST fluctuations can be identified in both the North Atlantic and North Pacific Oceans, including variations on timescales of decades (e.g., Wallace and Jiang 1987; Wallace et al. 1990; Douglas et al. 1982; Folland and Parker 1989; Trenberth 1990; Ghil and Vautard 1991; Deser and Blackmon 1993; Hurrell 1995; Zhang et al. 1997; Zhang and Levitus 1997). A mechanism for variability over a wide range of timescales is provided by the Hasselmann (1976) hypothesis. Representing the atmospheric internal variability as a stochastic process with short decorrelation times, the ocean is forced by random heat flux from the atmosphere. The upper ocean can convert the white noise forcing by the atmosphere into a red noise SST spectrum through its larger heat capacity (Hasselmann 1976; Frankignoul and Hasselmann 1977). Studies supporting the importance of atmospheric heat flux in forcing the ocean mixed layer include Frankignoul (1985), Alexander (1992a), Cayan (1992a), Battisti et al. (1995), Alexander and Penland (1996), Deser and Timlin (1997), and Hall and Manabe (1997). Cayan (1992a) and Deser and Timlin (1997) show that anomalous heat flux correlates well with the tendency of the SST anomalies

* University of California, Los Angeles, Institute of Geophysics and Planetary Physics Paper Number 4946.

Corresponding author address: Dr. J. David Neelin, Department of Atmospheric Sciences, UCLA, Los Angeles, CA 90095-1565.
E-mail: neelin@atmos.ucla.edu

in midlatitudes. This Hasselmann hypothesis mechanism is so simple and so prevalent that it can be viewed as a ''null hypothesis,'' and the question of the source of midlatitude SST variability becomes, what, if any, additional mechanisms are at play in interdecadal variability?

Various hypotheses for these additional mechanisms have been advanced. In the North Atlantic, some ocean modelers have focused on the role of internal ocean variability by thermohaline circulation variations, gyre instabilities, or ocean–ice interaction (e.g., Marotzke and Willebrand 1991; Weaver et al. 1991; Weaver and Sarachik 1991; Delworth et al. 1993; Winton and Sarachik 1993; Yang and Neelin 1993; Chen and Ghil 1995; Speich et al. 1995; Yang and Huang 1996). In the Pacific, where the El Niño–Southern Oscillation is active, some analyses suggest that tropical Pacific SST affects the midlatitude climate variability via the atmosphere (e.g., Luksch et al. 1990; Luksch and von Storch 1992; Alexander 1992a,b; Graham 1994; Trenberth and Hurrell 1994; Yukimoto et al. 1996; Zhang et al. 1996; Lau 1997), via the ocean (e.g., Jacobs et al. 1994), and possibly via two-way interaction (e.g., Gu and Philander 1997). Some hypotheses involve more complex processes within the ocean but rely, as in the Hasselmann hypothesis, on stochastic forcing by atmospheric internal variability (e.g., Frankignoul and Müller 1979; Weisse et al. 1994; Power et al. 1995; Delworth 1996; Frankignoul et al. 1997; Saravanan and McWilliams 1997, 1998; Zorita and Frankignoul 1997). Saravanan and McWilliams (1997) further point out that spatial correlations in the atmospheric forcing can play a crucial role in oceanic response. Hall and Manabe (1997) find a role for oceanic advection in contributing to low-frequency variability of SST, in addition to heat-flux forced variability. Luksch (1996) shows that anomalous ocean transports can be as important as heat fluxes in inducing SST anomalies in the Atlantic, especially around 40°N, and finds that a few atmospheric circulation patterns are responsible for most of the SST variability. Within the period 1950–79, she notes that there exist atmospheric anomalies and associated (modeled and observed) SST anomalies that persist for several years. Such timescales hint at variability that may not be purely atmospheric in origin.

It has been long known that the large-scale ocean–atmosphere interaction is important in natural climate variability over a broad range of timescales. In past years, much attention has focused on tropical air–sea interactions (e.g., Philander 1990; and references therein). The possibility of large-scale ocean–atmosphere interaction at midlatitudes had been proposed in the late 1950s and early 1960s (e.g., Namias 1959, 1963; Bjerknes 1962). It appears that large-scale interdecadal oscillations can be produced in coupled ocean–atmosphere general circulation models (GCMs) (e.g., von Storch 1994; Latif and Barnett 1994, 1996; Robertson 1996; Zorita and Frankignoul 1997; Grötzner et al. 1998). Latif and Barnett (1994, 1996) show evidence of coupled interdecadal variability in the North Pacific in a GCM study and suggest that the unstable air–sea interaction between the subtropical gyre circulation and the atmospheric circulation may play a role in producing this variability. In their model, SST variability is dominated by a large-scale positive SST anomaly pattern centered near 35°N and extending from the Asian coast across nearly the entire Pacific. The positive SST anomaly is surrounded by negative anomalies, most prominently in the south. The associated changes in the net surface heat flux are such that they tend to reinforce the SST anomalies over most of the North Pacific. Grötzner et al. (1998) find an interdecadal spectral peak in the Atlantic Ocean of the same coupled GCM, apparently with similar coupled mechanisms at work.

There is some question about the strength and complexity of the atmospheric response to midlatitude SST anomalies. Some atmospheric GCM experiments with prescribed midlatitude SST anomalies show a substantial response, thus suggesting a significant role for midlatitude SST (e.g., Palmer and Sun 1985; Pitcher et al. 1988; Lau and Nath 1990; Kushnir and Lau 1992; Ferranti et al. 1994; Peng et al. 1995; Peng et al. 1997). Other GCM experiments (e.g., Frankignoul 1985; Lau and Nath 1994; Kushnir and Held 1996) display only weak atmospheric response to midlatitude SST anomalies. These responses, either significant or weak, are potentially complicated and differ in different GCM experiments. Palmer and Sun (1985) found a surface high to the east northeast of a positive SST anomaly in the North Atlantic. A result qualitatively similar to Palmer and Sun was obtained by Peng et al. (1995) but only in their integrations with November conditions. Their integration with January conditions gave the opposite response, with a low downstream of a warm anomaly, explained by Ting and Peng (1995) as due to differences in climatological jet stream between these months. Lau and Nath (1990) examined the regression patterns of model geopotential height at various pressure levels versus the SST variations off the Newfoundland coast and northwest of Hawaii and suggested an equivalent barotropic response to midlatitude SST anomalies. However, the GCM experiments by Kushnir and Held (1996) display a baroclinic response to midlatitude SST.

In a study of ocean–atmosphere interaction in the North Atlantic, Kushnir (1994) suggested that at least two different modes of interaction exist, associated with interannual and interdecadal SST variability, respectively. He suggested that SST anomalies with interannual timescales display a coherent local relationship to the surface wind circulation. The observed correspondence between the pattern of wintertime SST tendency and SLP variability supports the notion that interannual SST variability is forced by the changing

pattern of the wintertime atmospheric circulation (Wallace et al. 1990; Cayan 1992a,b), akin to the Hasselmann hypothesis. In contrast, Kushnir suggests that interdecadal SST variability has a unique horizontal distribution that may be governed by a basin-scale dynamical interaction between the large-scale oceanic circulation and the atmosphere. This suggestion is similar to the hypothesis put forward by Bjerknes (1964).

Recently, several studies have been carried out in simple ocean–atmosphere coupled models to explore possible physical mechanisms of this basin-scale dynamical interaction in the midlatitude interdecadal climate variability (Miller 1992; Lui 1993; Jin 1997; Weng and Neelin 1997, 1998; Münnich et al. 1999). N. Schneider (1998, personal communication) considered the dependence of midlatitute decadal variability on a weak feedback between the ocean and atmospheric wind stress and a positive feedback between surface heat flux and SST. The important role of Rossby wave dynamics in the interdecadal mode is proposed by Jin (1997), Weng and Neelin (1997, 1998), and Münnich et al. (1999). Weng and Neelin (1997) further point out that the length scale of zonal wind stress also plays a crucial role in selecting the time and spatial scales of the mode.

Here, we present a simple ocean–atmosphere model (coupled or uncoupled) to investigate interdecadal climate variability in the North Atlantic and North Pacific Oceans. We examine a simple prototype for ''weather regime'' behavior (Kimoto and Ghil 1993a,b; Robertson and Ghil 1999) of the atmospheric response to SST anomalies by having the SST influence the statistics of a stochastic atmosphere model. We examine a stochastic process in which SST affects both the mean and variance of the atmospheric noise. We refer to this as an SST dependent stochastic process to emphasize the physical hypothesis that it embodies. We also use the term multiplicative noise to refer to aspects of this process, since stochastic processes that have a fundamental dependence on the state variables of the model are termed multiplicative (Gardiner 1985; Horsthemke and Lefever 1984). This differs from the additive noise processes of the Hasselmann (and related) hypothesis, in which the stochastic process is independent of SST and other model variables. We include a simple dependence of atmospheric probability density function on SST. Although simpler than the weather regime behavior found in a GCM by A. Robertson et al. (1998, personal communication), it permits a first evaluation of such effects. We compare the SST dependent noise atmosphere to deterministic atmospheric feedbacks, such as those examined in Weng and Neelin (1997, 1998).

The simple ocean–atmosphere model is described in sections 2 (ocean), 3 (atmosphere), and 4 (coupling). Section 5 examines the effect of SST dependent noise coupling by using a time integration method for both coupled and uncoupled systems. After examining the deterministic feedback as a limit of SST dependent noise in section 6, we reduce the atmosphere model to the additive stochastic forcing plus deterministic feedbacks. Then a near-analytic solution for the power spectrum is obtained and used to examine the effects of wind stress feedback and nonlocal heat flux feedback. Section 7 provides discussion and conclusions. In Weng and Neelin 1999, (Part II of this paper), we shall present eigenmodes of the deterministic coupled system and examine its near-analytical solutions, which provide prototypes for discussing the selection of time and spatial scales of the interdecadal modes in the coupled system.

2. Simple ocean model

We consider a linearized perturbation system with quasigeostrophic shallow water upper-ocean dynamics and an SST equation for a surface mixed layer. The equations are written on a β plane with mean latitude at 40°N. Linearizing about a basic state with realistic gyres could potentially give instabilities with complicated dynamics even in the ocean alone (Speich et al. 1995). Since we wish to focus on processes arising from interaction with the atmosphere, we choose to linearize about a state of rest in the ocean dynamics, although we include basic-state gradients of SST. For oceanic motions generated by wind stress, the linearized quasigeostrophic vorticity equation is

$$\partial_t(\nabla^2 - \lambda^{-2})\psi_g + \beta\partial_x\psi_g = \partial_x\left(\frac{\tau^y}{\rho H}\right) - \partial_y\left(\frac{\tau^x}{\rho H}\right) - \epsilon_c\nabla^2\psi_g + \nu\nabla^4\psi_g, \quad (2.1)$$

where $\nabla^2 = \partial_x^2 + \partial_y^2$; $\lambda = c_0/f_0 = \sqrt{g^*H}/f_0$ is the Rossby deformation radius. The mean depth of the upper layer H is assumed to be 100 m, g^* is the reduced gravity and is chosen to give a wave speed c_0 about 3 m s^{-1}, and f_0 is the Coriolis parameter at 40°N. These give the Rossby deformation radius about 32 km. The latitudinal derivative of the Coriolis parameter β is fixed at the 40°N value, ψ_g is the geostrophic streamfunction of the upper layer, ρ the upper-layer seawater density, and τ^x and τ^y the zonal and meridional components of wind stress, respectively. For damping terms, we include a Rayleigh damping applied to ocean current, of rate ϵ_c, for which we test values between 0 and 1 yr^{-1}, and a horizontal turbulent viscosity coefficient, ν, with values in the range 10 to 10^4 m^2 s^{-1} (Pedlosky 1987). The effect of uncertainty associated with the values of ϵ_c and ν will be examined.

Linearizing the advection terms about a basic state of rest, the SST anomaly equation for the mixed layer is

$$\partial_t T = -(u\partial_x\overline{T} + v\partial_y\overline{T}) + Q, \quad (2.2)$$

where T is the perturbation temperature of sea surface mixed layer and $\overline{T}$ the climatological temperature of the mixed layer, which is approximated by the observed

climatological SST in both oceans. The heat source or sink, Q, we consider to be due to the net heat flux across the air–sea interface divided by the heat capacity of the layer. For brevity, we refer to this as the heat flux.

In addition to the geostrophic currents $u_g = -\partial_y \psi_g$ and $v_g = \partial_x \psi_g$, we include Ekman currents, approximated for a mixed layer of fixed depth, H_1,

$$u_E = \frac{\tau^y}{f\rho H_1} \tag{2.3}$$

$$v_E = -\frac{\tau^x}{f\rho H_1}, \tag{2.4}$$

where f is the Coriolis parameter. SST is advected by surface currents that are the sum of the two. The SST anomaly equation then becomes

$$\partial_t T = (\partial_x \overline{T}\partial_y - \partial_y \overline{T}\partial_x)\psi_g - \left(\frac{\tau^y}{f\rho H_1}\partial_x - \frac{\tau^x}{f\rho H_1}\partial_y\right)\overline{T} + Q. \tag{2.5}$$

Equations (2.1) and (2.5) form our ocean model, which is coupled to the atmosphere through wind stress and heat flux as discussed in the next section.

3. Stochastic atmospheric model

a. Approach

The internal variability of the midlatitude atmosphere tends to be uncorrelated on timescales longer than about a month, and variability associated with storms is poorly correlated on timescales longer than a week. One representation of this would be white noise in time, as in the Hasselmann (1976) hypothesis, with large-scale, potentially complicated correlation patterns in space. Much of this atmospheric variability is independent of SST variations. We model this as the atmospheric additive noise stochastic forcing F_a (either wind stress or heat flux):

$$F_a(x, y, t) = \sum_{j=1}^{J} F_{aj}(x, y)\xi_{aj}(t), \tag{3.1}$$

where subscript a represents additive and F_{aj} is the jth spatial pattern. Here, ξ_{aj} is the jth random variable whose probability density function (PDF) is assumed Gaussian with zero mean and standard deviation s_{aj}. We approximate the standard deviation by the plausible magnitude of the corresponding climate variable. Since our model is linear, accurate estimate of this value is not crucial in the sense that it only affects the magnitude.

As discussed in section 1, we postulate that the probability density function of large-scale weather patterns may be influenced by SST. Here we want a simple prototype for such complex behavior. While in reality such SST dependent noise should depend on the seasonal cycle, here we omit this for simplicity. Consider the SST anomaly T, represented in terms of spatial basis functions θ_n, of which θ_1 is the leading one of the series and the rest are orthogonal. That is,

$$T = \sum_{n=1}^{N} \theta_n(x, y)T_n(t), \tag{3.2}$$

where T_n is the scalar coefficient of the nth SST basis function θ_n.

For a stochastic process F_s in which we hypothesize that the PDF of random atmospheric variables is affected by SST, we expand a general dependence of F_s in a Taylor series in T. The linear term will tend to dominate for small SST anomalies, leading to a form

$$F_s(x, y, t) = \sum_{n=1}^{N} F_{sn}(x, y)\xi_{sn}(t)T_n,$$

where subscript s represents SST dependence, F_{sn} is the nth spatial pattern, and ξ_{sn} is the nth random variable. We expect ξ_{sn} to have both a mean and a standard deviation. It will be useful to consider the mean separately to examine the deterministic limit of this stochastic process, so we write, without loss of generality,

$$F_s(x, y, t) = \sum_{n=1}^{N} F_{sn}(x, y)(1 + \xi_{mn})T_n. \tag{3.3}$$

The term $\xi_{mn}T_n$ is termed a multiplicative noise (hence the subscript m) since it contains the dependence of the stochastic forcing on SST in a fundamental way. It produces an SST dependence in the variance of F_s. Constants of proportionality have been absorbed into the nth spatial pattern F_{sn}, and for the associated nth random variable ξ_{mn} we assume its PDF has a Gaussian distribution with standard deviation $\tilde{s}_{mn}$. The mean of ξ_{mn} is zero by construction. In the limiting case where $\tilde{s}_{mn}$ goes to zero for all n, F_s becomes $\sum_{n=1}^{N} F_{sn}T_n$, which yields deterministic feedbacks expressed as the spatial patterns associated with SST projections.

We will refer to the standard deviation of the multiplicative noise process both nondimensionally and dimensionally. The importance of the multiplicative noise term within F_s depends on the size of $\tilde{s}_{mn}$ compared to 1 [due to the term $(1 + \xi_{mn})$]. In comparing potential effects of multiplicative noise with the additive noise, it is useful to have a measure of $\tilde{s}_{mn}$ in dimensional terms. We define

$$s_{mn} = \max[F_{sn}(x, y)]\sigma_n\tilde{s}_{mn}, \tag{3.4}$$

where σ_n is a typical magnitude of T_n (e.g., the standard deviation of T_n from the observed SST record).

If we consider that wind stress forcing is composed of additive and SST dependent forcing and that heat flux forcing includes also a local heat flux feedback ($-\epsilon_T T$, where ϵ_T is the decay rate), in addition to additive and SST dependent forcing, then we have, replacing F in the above form with each variable of interest,

$$\tau^x = \mu \sum_{n=1}^{N} \tau^x_{sn}(x, y)[1 + \xi^\tau_{mn}(t)]T_n(t) + \sum_{j=1}^{J} \tau^x_{aj}(x, y)\xi^\tau_{aj}(t) \quad (3.5)$$

$$\tau^y = \mu \sum_{n=1}^{N} \tau^y_{sn}(x, y)[1 + \xi^\tau_{mn}(t)]T_n(t) + \sum_{j=1}^{J} \tau^y_{aj}(x, y)\xi^\tau_{aj}(t) \quad (3.6)$$

$$Q = -\epsilon_T T + \frac{\mu}{c_w \rho H_1} \sum_{n=1}^{N} Q_{sn}(x, y)[1 + \xi^Q_{mn}(t)]T_n(t) + \frac{1}{c_w \rho H_1} \sum_{j=1}^{J} Q_{aj}(x, y)\xi^Q_{aj}(t), \quad (3.7)$$

where superscripts x and y represent the zonal and meridional components of wind stress patterns, respectively. The superscripts τ and Q indicate that the random variables are for wind stress and heat flux, respectively. The depth of the sea surface mixed layer H_1 is 50 m in our model and c_w is the specific heat of seawater. The heat flux is defined to be positive into the ocean. The relative coupling coefficient μ is introduced for the purpose of testing the effect of SST-dependent terms.

To include the effect of correlation on timescales shorter than about a week, each of the random variables given in (3.5)–(3.7) is expressed by

$$\xi(t) = \kappa\xi(t - \Delta t) + \hat{\xi}, \quad (3.8)$$

where $\kappa = e^{-\Delta t/t_{\rm corr}}$ comes from integrating

$$d\xi = -t^{-1}_{\rm corr}\xi dt + D\, dw \quad (3.9)$$

over one time step Δt of the numerical implementation. Here $t_{\rm corr}$ is the correlation time assumed for the ''weather'' noise process and dw is a Wiener process. The initial condition for $\hat{\xi}$ *is zero. Both* $\hat{\xi}$ *and* ξ are Gaussian distributed with zero mean and standard deviations $\hat{s}$ and s given respectively by

$$s = \hat{s}(1 - \kappa^2)^{-1/2} = D(t_{\rm corr}/2)^{1/2}. \quad (3.10)$$

We choose a standard deviation for s, and set D for $t_{\rm corr} = 5$ days. Note that $\hat{s}$ depends on time step such that s is independent of time step.

Since there is no good estimate of the standard deviation of multiplicative noise, we test values of s_{mn} between zero and twice the standard deviation of the corresponding additive noise. We note that when the multiplicative and additive noise components are combined, the overall standard deviation of the PDF varies with T_n.

Figure 1 shows the PDF of the first atmospheric wind stress forcing patterns when $s^\tau_{a1} = 0.4$ dyn cm^{-2} (crudely estimated based on da Silva et al. 1994) and $s^\tau_{m1} = 0.2$ dyn cm^{-2} (which is the standard value used in most runs). The solid line is for additive noise only and the dashed line for the sum of additive and SST dependent noise for the case of $T_1 = 2.14$ (nondimensional). This value simply illustrates the PDF change for a ''typical'' amplitude of the first SST pattern, in this case the standard deviation of the projection of the Atlantic case basis function discussed below. This figure shows that the postulated effect of an SST anomaly on the noise is a very modest change of the PDF compared to the additive noise. An effect this small would not be easy to evaluate directly from data, and yet we will show it can have significant effects. It should be possible to evaluate such PDF changes from GCM data but this would require a large ensemble of experiments. We note that the departure from Gaussian form in both curves in Fig. 1 is due to sampling. We have purposefully chosen a sample that is large (400 yr of daily data) compared to most datasets in order to illustrate the sampling effects. For a larger sample both curves converge to Gaussian distribution when T_1 is fixed, since the sum of the mutually independent Gaussian variables has Gaussian distribution (when T_1 varies in a way that depends on the noise this need not hold.) In the case with SST dependent noise, the mean is T_1 and the standard deviation is given by $(s^2_{a1} + T^2_1 s^2_{m1})^{1/2}$. Note that both the mean and standard deviation depend on SST. The value of s^τ_{m1} (=0.2 dyn cm^{-1}) used in Fig. 1 corresponds to a nondimensional value of $\tilde{s}^\tau_{m1} = 2$. In the SST dependent noise, the random variable $\xi_{sn} = (1 + \xi_{mn})$ has a mean of 1, so this value of the standard deviation is large compared to the mean. In this sense, the postulated SST dependence is very noisy.

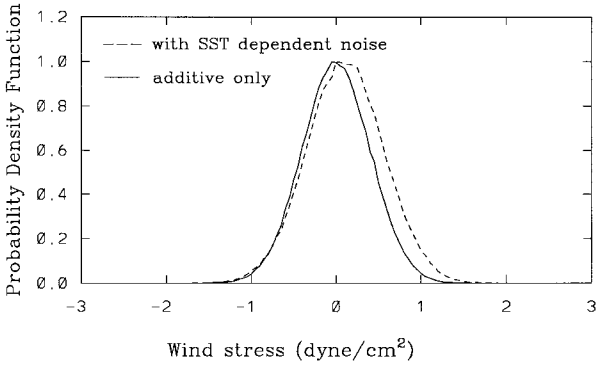

FIG. 1. Atmospheric model probability density function for the North Atlantic case. Additive noise versus additive plus SST dependent noise for an SST pattern with typical amplitude (one standard deviation of T_1).

Peng et al. (1997) show histograms akin to Fig. 1 from GCM control and Pacific anomaly experiments with ensembles of 384 months, and this appears to be almost adequate to distinguish between the distributions. The shift between their histograms for anomaly and control cases appears comparable to the PDF we postulate in Fig. 1 (although they display pattern correlations rather than projections). A. Robertson et al. (1998, personal

communication) estimate weather regimes from a 100-yr control run and find three regimes that show excursions in frequency of about one standard deviation in an Atlantic SST anomaly experiment. In the most strongly affected regime, the pattern occurs only about half as often in the anomaly run as in the control. The simple form for the change in the PDF that we use may not capture all such effects.

In the limit that all s_{aj} and s_{mn} go to zero, our atmospheric model [Eqs. (3.5)–(3.7)] becomes deterministic. That is,

$$\tau^x = \mu \sum_{n=1}^{N} \tau^x_{sn} \frac{\langle \theta_n T \rangle}{\langle \theta_n^2 \rangle} \tag{3.11}$$

$$\tau^y = \mu \sum_{n=1}^{N} \tau^y_{sn} \frac{\langle \theta_n T \rangle}{\langle \theta_n^2 \rangle} \tag{3.12}$$

$$Q = -\epsilon_T T + \frac{\mu}{c_w \rho H_1} \sum_{n=1}^{N} Q_{sn} \frac{\langle \theta_n T \rangle}{\langle \theta_n^2 \rangle}, \tag{3.13}$$

where T_n is replaced by $\langle \theta_n T \rangle / \langle \theta_n^2 \rangle$, and $\langle \theta_n T \rangle$ is the nth SST projection, which is defined as an inner product over space (within the basin) of the spatial pattern of SST with the nth SST basis function. In this limit, we can think of the terms on the right-hand sides of (3.11) to (3.13) as the deterministic feedbacks from the atmosphere to the ocean. Here, τ^x_{sn}, τ^y_{sn}, and Q_{sn} are the nth spatial feedback patterns of zonal component of wind stress, meridional component of wind stress, and nonlocal heat flux per SST projection, respectively. The artificial parameter μ controls the strength of the nonlocal feedback from the atmosphere to the ocean relative to its standard value. The model is uncoupled when $\mu = 0$, and has standard coupling when $\mu = 1$.

Equations (3.5)–(3.8) form the stochastic atmospheric model. In the following subsections, we discuss the estimation of the spatial wind stress and heat flux feedback patterns based on the analyses of GCM results and observations (e.g., Wallace et al. 1990; Deser and Blackmon 1993; Hense et al. 1990).

b. Estimates of spatial feedback patterns

We require plausible estimates of spatial patterns in the atmospheric response that are associated with a given pattern of SST. In observations, it is ambiguous whether the atmosphere is driving the ocean or vice versa, so we turn to atmospheric GCM (AGCM) experiments where it is clearer that the specified SST is driving the atmospheric response if the two are significantly correlated. AGCM experiments with a fixed pattern of SST can potentially provide such an association of SST to response. AGCM experiments with interannually varying observed SST can likewise be used by seeking statistical relations of the response to the forcing. In this latter method, possible correlation between tropical and extratropical SST requires caution in interpretation of the atmospheric response for the Pacific case (Graham et al. 1994; Lau and Nath 1994). Since we intend to examine sensitivity to such feedbacks for various idealized patterns, we only need rough estimates of the magnitude of the response and plausible spatial structures.

For the case of heat flux feedback, a highly truncated series representation risks distorting the essential negative feedback of heat flux on SST that must hold over large enough regions. We therefore approximate the heat flux feedback in two parts: a simple local negative feedback ($-\epsilon_T T$) and nonlocal heat flux feedbacks [the terms on the rhs of equation (3.13) except $-\epsilon_T T$]. The local regression coefficient of heat flux on SST, point to point everywhere on the globe was computed. To get a basic feedback for heat flux, the average of the regression coefficient over the North Atlantic or the North Pacific was calculated. This is about -17 W (m^2 K)$^{-1}$ over either area, estimated from the Hamburg version of the ECMWF T21 atmospheric model (ECHAM2) forced with observed global SST over the period 1970–88. This gives a basic negative heat flux feedback in both oceans. The decay rate for the local heat flux feedback, ϵ_T, is obtained by dividing -17 W (m^2 K)$^{-1}$ by the heat capacity of the mixed layer. With 50-m constant mixed layer depth, ϵ_T is about 2.73 yr^{-1}.

By subtracting the basic negative heat flux from the time series of net surface heat flux and regressing the remainder on the nth SST projection, we obtain the nth heat flux feedback pattern, which is the spatial distribution of linear regression coefficients between the nth SST projection and the remainder of the heat flux. Similarly, wind stress feedback patterns are obtained as the spatial distribution of linear regression coefficients between the nth SST projection and the wind stress components.

c. North Atlantic case

The response of the ECHAM2 AGCM to interannual SST has been analyzed by Graham et al. (1994) and Kharin (1995). The analysis here is related to the latter. SST basis functions are obtained by canonical correlation analysis (CCA; see Barnett and Preisendorfer 1987; Bretherton et al. 1992) between SST and mean sea level pressure (SLP). Five EOFs are retained in the CCA analysis, which is simply used to select an SST pattern that correlates strongly with AGCM variability.

The CCA of SST and SLP shows one clearly defined SST pattern (Fig. 2a), which correlates well with coherent atmospheric response on the North Atlantic domain. This SST basis function has an approximate north–south dipole pattern with a negative and a positive SST anomaly, centered near 30° and 50°N, respectively. Both centers have maximum anomalies in the western Atlantic. This pattern is similar to that examined by, for instance, Wallace et al. (1990), Zorita et al. (1992), and Kharin (1995) where statistical significance is examined. We use only this leading mode

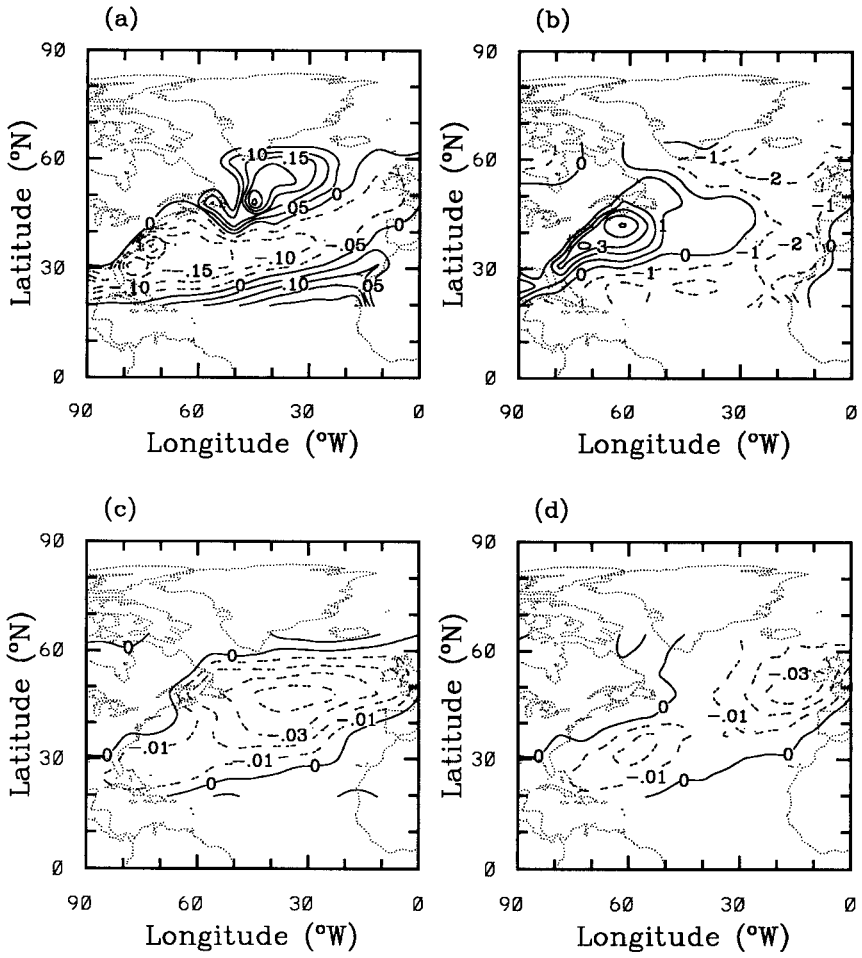

FIG. 2. (a) The first SST basis function (contour interval 0.05 K), (b) the nonlocal heat flux feedback (contour interval 1 W m^{-2}), (c) the zonal component of wind stress feedback (contour interval 0.01 dyn cm^{-2}), and (d) the meridional component of wind stress feedback (contour interval 0.01 dyn cm^{-2}) over the North Atlantic.

to compute atmospheric feedback patterns of wind stress and nonlocal heat flux over the North Atlantic domain. These are determined by regression of heat flux (subtracting the local feedback term) and wind stress onto the SST projection on the CCA mode pattern, using the full year monthly mean for the period from 1970 to 1988.

The nonlocal heat flux feedback pattern is given in Fig. 2b, which shows large positive anomalies over most of the western North Atlantic, decreasing toward the east. The zonal component of wind stress feedback pattern (Fig. 2c) is mostly negative, minimum at about 45°N, 35°W. The meridional component of wind stress feedback (Fig. 2d) is small over the central North Atlantic. The corresponding wind stress curl has a positive maximum near 30°N and a negative minimum near 60°N (Fig. 3). In our simple model, we consider an idealized basin with latitude from 20° to 60°N and longitude from 70° to 10°W in the North Atlantic. We thus stretch the first SST basis function, heat flux feedback, and wind stress feedback from the original basin onto a rectangular basin such that the basic features of the original fields are maintained. The resulting fields for the first SST basis function and the heat flux feedback, obtained by aligning the western boundary at the same longitude, and stretching the fields accordingly, are shown in Weng and Neelin (1998, their Fig. 1).

The effect on ocean current of further simplifying spatial wind stress patterns was tested by spinning up the ocean current with steady wind stress to steady state. We compared results using 1) the wind stress pattern given in Figs. 2c and 2d; 2) the zonal component of wind stress given in Fig. 2c, but with a meridional component of zero; and 3) using a simplified sinusoidal approximation to Fig. 2c. The final steady states of the geostrophic streamfunction for these cases are very similar. Based on this, we simplify the wind stress feedback pattern by assuming a sinusoid pattern for the zonal component and zero field for the meridional component. That is,

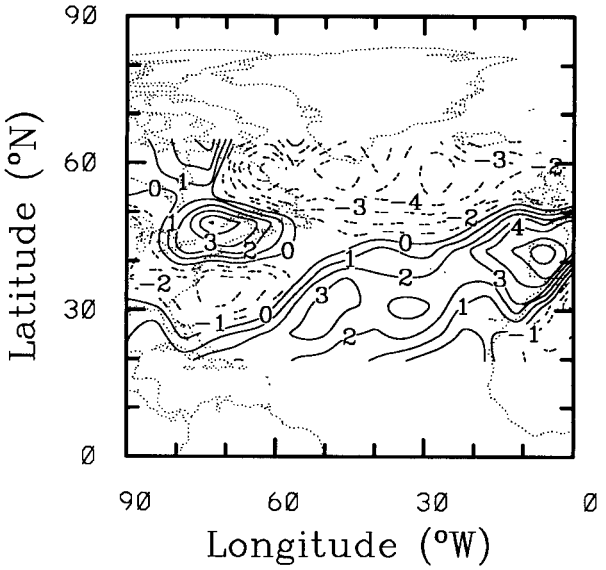

FIG. 3. The curl of wind stress feedback (labels in units of 10^{-9} N m^{-3}; contour interval 10^{-9} N m^{-3}) over the North Atlantic.

$$\tau^x_{s1} = \cos(ly + \gamma)\tau_{s1}(x) \tag{3.14}$$

$$\tau^y_{s1} = 0, \tag{3.15}$$

where

$$\tau_{s1}(x) = \tau_A \cos(kx + \alpha), \tag{3.16}$$

and τ_A is the amplitude of the zonal component of wind stress feedback; k and l are the zonal and meridional wavenumbers of the wind stress, respectively; $x = 0$ at western boundary and $x = L_x$ at eastern boundary; and α and γ are the zonal and meridional phases of the zonal wind stress feedback, respectively. Based on Fig. 2c, we estimated that $\alpha = 0.5\pi$, $\gamma = -0.8\pi$, $\tau_A = 0.05$ dyn cm^{-2}, $k = 3/[R\cos(40°)]$, and $l = 6/R$, where R is the radius of earth. With these parameters, the wind stress curl obtained from (3.14) to (3.16) has a spatial pattern similar to that over the irregular Atlantic basin in the sense that the wind stress curl has a positive maximum near 30°N and a negative minimum near 60°N. We also treat more general functions of x for sensitivity testing, as discussed in section 6.

In order that a near-analytic solution can be found, we similarly simplify the spatial pattern for additive wind stress forcing as

$$\tau^x_{aj} = \cos(ly + \gamma)\tau_{aj}(x) \quad \text{for } j = 1, 2, \ldots, J \tag{3.17}$$

$$\tau^y_{aj} = 0 \quad \text{for } j = 1, 2, \ldots, J. \tag{3.18}$$

By substituting Eqs. (3.14), (3.15), (3.17), and (3.18) into Eqs. (3.5) to (3.7), our atmospheric model becomes

$$\tau^x = \cos(ly + \gamma)\left\{\mu\tau_{s1}(x)[1 + \xi^\tau_{m1}(t)]T_1 + \sum_{j=1}^{J} \tau_{aj}(x)\xi^\tau_{aj}(t)\right\} \tag{3.19}$$

$$\tau^y = 0 \tag{3.20}$$

$$Q = -\epsilon_T T + \frac{1}{c_w \rho H_1}\left\{\mu Q_{s1}(x, y)[1 + \xi^Q_{m1}(t)]T_1 + \sum_{j=1}^{J} Q_{aj}\xi^Q_{aj}(t)\right\}. \tag{3.21}$$

d. North Pacific case

Similar to the North Atlantic case, we consider an idealized North Pacific basin with latitude from 20° to 60°N and longitude from 140°E to 121°W. The SST basis function, wind stress feedback, and heat flux feedback pattern are estimated based on results of the AGCM experiments by Lau and Nath (1990) and Latif and Barnett (1994).

In a GCM experiment on atmospheric response to midlatitude SST anomalies, Lau and Nath (1990) examined regression charts of SST, surface heat flux, and geopotential height at various levels versus the SST variations off the northwest of Hawaii. The regression map of SST exhibits anomalies of one sign in the central North Pacific extending into the western Pacific along about 40°N and anomalies of the opposite sign along the coast of North America. SST patterns similar to this are also obtained by Weare et al. (1976), Folland and Parker (1989), and Namias et al. (1988). Their regression coefficients for heat flux have a large-scale positive anomaly dominating over the western and central North Pacific, with a positive maximum centered near 35°N, 170°W. This positive anomaly is surrounded by negative anomalies. The regression chart of geopotential height near the surface has a large-scale anticyclone over the east of North Pacific. We use these regression charts (Figs. 12c, 13a, and 13c in Lau and Nath 1990) to estimate the SST and feedback patterns for use in our model. Figure 4 shows the SST basis function and the heat flux feedback for the idealized North Pacific basin. These two fields were estimated such that they are similar to those obtained by Lau and Nath (1990) (note differing sign convention for heat flux). Based on Lau and Nath's (1990) Fig. 12c of geopotential height at 990 mb, we estimate $\tau_A = 0.2$ dyn cm^{-2} (using drag coefficient $C_D = 0.0012$), $\alpha = 0.075\pi$, $\gamma = -0.325\pi$, $2\pi/k$ about 13 600 km, and $2\pi/l$ about 8900 km. Note that this magnitude of feedback is comparable to the Atlantic case when the normalization of the basis functions is taken into account, since θ_1 in Fig. 4a for the Lau and Nath case is about three times as large as θ_1 in Fig. 2a for the Atlantic case.

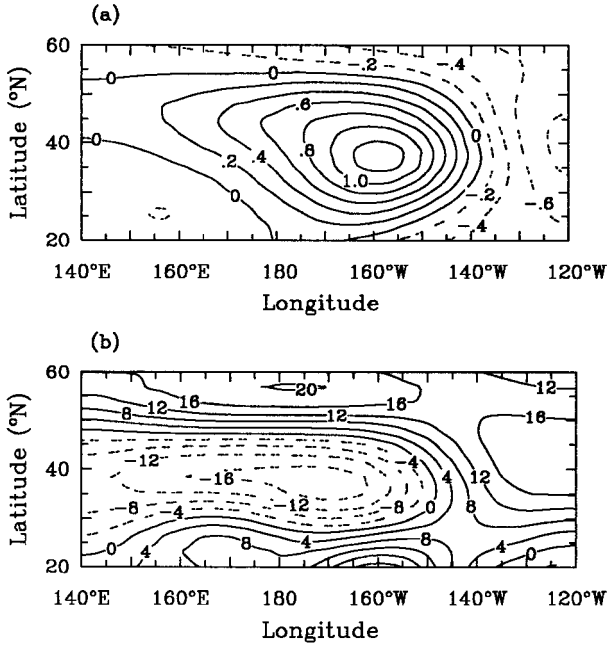

FIG. 4. (a) The SST basis function (contour interval 0.2 K), and (b) the heat flux feedback pattern (contour interval 4 W m^{-2}) used in the North Pacific ''Lau and Nath'' case. Based on Lau and Nath (1990) distributions of the linear regression coefficients between SST variations northwest of Hawaii with SST anomaly, and sum of AGCM latent and sensible heat flux, respectively. Their patterns are stretched to a rectangular Pacific domain.

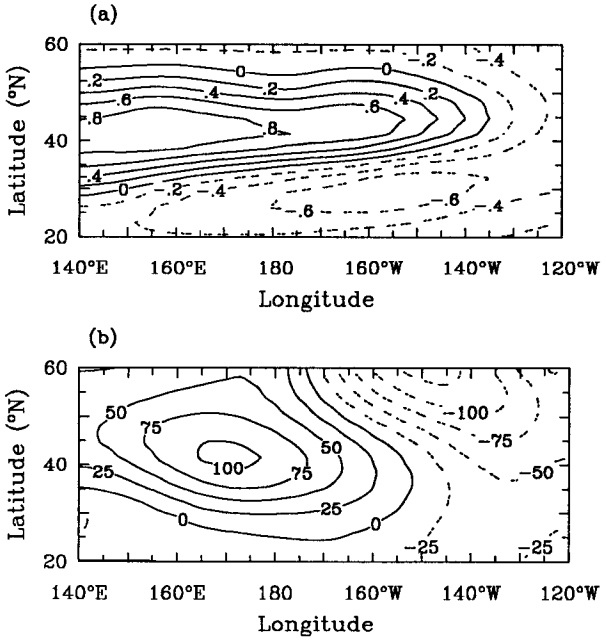

FIG. 5. (a) The SST basis function (contour interval 0.2 K) and (b) the heat flux feedback pattern (contour interval 25 W m^{-2}) used in the North Pacific ''Latif and Barnett'' case. Based on Latif and Barnett (1994) fields, stretched to a rectangular Pacific domain. In (a) the spatial distribution of linear regression coefficients between the index time series shown in Fig. 1a of Latif and Barnett (1994) and SST values are used. In (b) the atmospheric GCM response of net surface heat flux to the SST anomaly shown in their Fig. 6a is used.

In the study of climate variability over the North Pacific, Latif and Barnett (1994) use a coupled GCM to simulate the interdecadal climate variability in the North Pacific. They found decadal-scale SST variability having large-scale spatial patterns as discussed in the introduction. They present the associated wind stress curl, evaluated from an AGCM run with specified SST anomaly. Figures 5a and 5b are estimated based on the Figs. 1b and 3b, respectively, given by Latif and Barnett (1994). The zonal wind stress feedback pattern is estimated based on their Fig. 3c of wind stress curl, which gives $\tau_A = 2$ dyn cm^{-2}, $\alpha = 0.375\pi$, $\gamma = -0.67\pi$, $2\pi/k$ is about 13 600 km, and $2\pi/l$ about 6700 km. This is a stronger feedback than the Lau and Nath case: since the SST basis function θ_1 in Fig. 5a is comparable in magnitude to the Lau and Nath θ_1 in Fig. 4a, τ_A can be compared directly to the Lau and Nath τ_A of 0.2 dyn cm^{-2}.

4. The coupled model

Equations (2.1), (2.5), (3.8), (3.19), (3.20), and (3.21) form a simple coupled model. With the simplified wind stress form in (3.19) and (3.20), we assume that the dependence of ψ_g on y can be separated from other variables associated with feedbacks and approximate it as

$$\psi_g(x, y, t) = \psi(x, t)\sin(ly + \gamma). \tag{4.1}$$

Then our coupled model becomes

$$[\partial_t(\partial_x^2 - l^2 - \lambda^{-2}) + \beta\partial_x + \epsilon_c(\partial_x^2 - l^2) - \nu(\partial_x^2 - l^2)^2]\psi = \frac{l}{\rho H}\left\{\mu\tau_{s1}(x)[1 + \xi^{\tau}_{m1}(t)]\frac{\langle\theta_1 T\rangle}{\langle\theta_1^2\rangle} + \sum_{j=1}^{J}\tau_{aj}(x)\xi^{\tau}_{aj}(t)\right\} \tag{4.2}$$

$$\partial_t T = -\epsilon_T T + [l\cos(ly + \gamma)\partial_x\overline{T} - \sin(ly + \gamma)\partial_y\overline{T}\partial_x]\psi + \frac{\cos(ly + \gamma)\partial_y\overline{T}}{f\rho H_1}\times\left\{\mu\tau_{s1}(x)[1 + \xi^{\tau}_{m1}(t)]\frac{\langle\theta_1 T\rangle}{\langle\theta_1^2\rangle} + \sum_{j=1}^{J}\tau_{aj}(x)\xi^{\tau}_{aj}(t)\right\} + \frac{1}{c_w\rho H_1}\left\{\mu Q_{s1}(x, y)[1 + \xi^{Q}_{m1}(t)]\frac{\langle\theta_1 T\rangle}{\langle\theta_1^2\rangle} + \sum_{j=1}^{J}Q_{aj}\xi^{Q}_{aj}(t)\right\}, \tag{4.3}$$

where T_1 has been replaced by $\langle\theta_1 T\rangle/\langle\theta_1^2\rangle$. The random variables in (4.2) and (4.3) are given by (3.8). In the results presented, we use a correlation time $t_{\text{corr}} = 5$ days for the random variables ξ^{τ}_{m1}, ξ^{Q}_{m1}, ξ^{τ}_{aj}, and ξ^{Q}_{aj} for j

$= 1, 2, \ldots, J$. In practice, we sometimes use a random zonal phase for sinusoidal patterns in the spatial basis functions $\tau_{aj}(x)$, rather than fixed patterns (although formally these are equivalent if correlations among ξ_{aj} are suitably treated).

In the limiting case where the standard deviations of the multiplicative noise components go to zero, we have

$$[\partial_t(\partial_x^2 - l^2 - \lambda^{-2}) + \beta\partial_x + \epsilon_c(\partial_x^2 - l^2) - \nu(\partial_x^2 - l^2)^2]\psi = \frac{l}{\rho H}\left[\mu\tau_{s1}(x)\frac{\langle\theta_1 T\rangle}{\langle\theta_1^2\rangle} + \sum_{j=1}^{J}\tau_{aj}(x)\xi_{aj}^{\tau}(t)\right] \quad (4.4)$$

$$\partial_t T = -\epsilon_T T + [l\cos(ly+\gamma)\partial_x\overline{T} - \sin(ly+\gamma)\partial_y\overline{T}\partial_x]\psi + \frac{\cos(ly+\gamma)\partial_y\overline{T}}{f\rho H_1}\left[\mu\tau_{s1}(x)\frac{\langle\theta_1 T\rangle}{\langle\theta_1^2\rangle} + \sum_{j=1}^{J}\tau_{aj}(x)\xi_{aj}^{\tau}(t)\right] + \frac{1}{c_w\rho H_1}\left[\mu Q_{s1}(x,y)\frac{\langle\theta_1 T\rangle}{\langle\theta_1^2\rangle} + \sum_{j=1}^{J}Q_{aj}\xi_{aj}^{Q}(t)\right]. \quad (4.5)$$

In this limit of the multiplicative noise case, the atmospheric model reverts to a case similar to that treated in Weng and Neelin (1997, 1998), with deterministic feedbacks and additive noise.

5. Effects of SST dependent noise coupling

To investigate the effects of SST dependent noise, a time-marching method is used to solve the coupled model given by Eqs. (4.2) and (4.3), where τ_{s1} is given by Eq. (3.16). This form is considered as the prototype for a case where storm track statistics depend on SST. The large-scale additive wind stress forcing has a sinusoid spatial pattern with a wave number the same as that of the wind stress feedback but with random phase uniformly distributed in the zonal direction between 0 and 2π. The additive heat flux forcing has a spatial pattern the same as the heat flux feedback pattern. Both multiplicative and additive noise contributions have a 5-day autocorrelation in time, that is, they are red for frequencies higher than $(5\text{ day})^{-1}$ and white for lower frequencies. The model horizontal resolution is 0.5° for the vorticity equation and 3° for the SST equation. The integration starts from zero initial perturbation and has a time step of one day.

The standard deviations used for atmospheric additive wind stress forcing, s_{a1}^{τ}, are 0.4 dyn cm^{-2} over the North Atlantic and 0.3 dyn cm^{-2} over the North Pacific. These values are crudely estimated based on the da Silva et al. (1994) wind stress standard deviations, but we note the caveat that many spatial scales contribute to the observed standard deviation, whereas we include only large-scale patterns. The standard deviation of atmospheric multiplicative wind stress forcing, s_{m1}^{τ}, is 0.2 dyn cm^{-2} over both oceans. We discuss the effect of this variable in the next section. Typical standard deviations for monthly heat flux, given by da Silva et al. (1994), are on the order of 30 W m^{-2}. When we apply this to a single spatial pattern of the heat flux additive noise, the associated EOF dominates the time series (as shown below). While it may be realistic that heat flux effect on SST dominates short correlation timescales, we are interested in seeing modes associated with long timescales more clearly. Furthermore, partitioning among different spatial patterns should reduce the standard deviation associated with a given pattern. We thus decrease the additive heat flux standard deviation, s_{a1}^{Q}, to 5 W m^{-2} for most of the runs presented. We test different standard deviations of multiplicative heat flux forcing, s_{m1}^{Q}, in the next section, but we use 2 W m^{-2} as the standard.

a. North Atlantic

A 1000-yr coupled integration ($\mu = 1$) is conducted over the North Atlantic. We randomly choose an 80-yr time series from this run, showing geostrophic streamfunction and SST anomalies along 50°N in Fig. 6. Even without statistical techniques, interdecadal oscillations may be seen in both time series. The maximum SST anomaly is about 0.4°C. Geostrophic streamfunction anomalies tend to propagate to the west. In SST anomalies, propagation is less clear, but the interdecadal timescale associated with streamfunction anomalies can be picked out.

Empirical orthogonal functions (EOFs) of the geostrophic streamfunction and SST anomalies are computed based on the 1000-yr coupled integration over the domain (Fig. 7). The spatial patterns of EOF 1 and EOF 2 of the SST anomalies account for 44% and 20% of the variance of SST anomalies over the domain, respectively (Figs. 7a,c). Both patterns have large-scale north–south dipole patterns. EOF 1 and EOF 2 of the geostrophic streamfunction explain 71% and 22% of the variance of the geostrophic streamfunction, respectively (Figs. 7b,d). Both of them have a smooth large-scale pattern that decays eastward. SST and streamfunction EOFs are calculated separately. In this case, they are closely related, with a correlation of 0.87 between SST-EOF 1 and ψ-EOF 1 and of 0.92 between SST-EOF 2 and ψ-EOF 2.

We examined the power spectra of the leading EOFs using the maximum entropy method (MEM). Unless otherwise stated a MEM order of 10 is used and we have examined sensitivity to the MEM order. To provide a measure of statistical significance, three 1000-yr coupled integrations are conducted, each with a different sequence of random variables. There are power spectral peaks at periods around 16 yr for EOF 1 and 11 years for EOF 2 of geostrophic streamfunction and at period around 12 yr for EOF 1 and EOF 2 of SST anomalies (Fig. 8). Power spectra for sum-of-square SST or streamfunction are shown in section 6; EOF spectra are shown here to distinguish variability associated with important spatial patterns. Peaks tend to be less distinct when not filtered by EOFs, since they are mixed in with red noise variability.

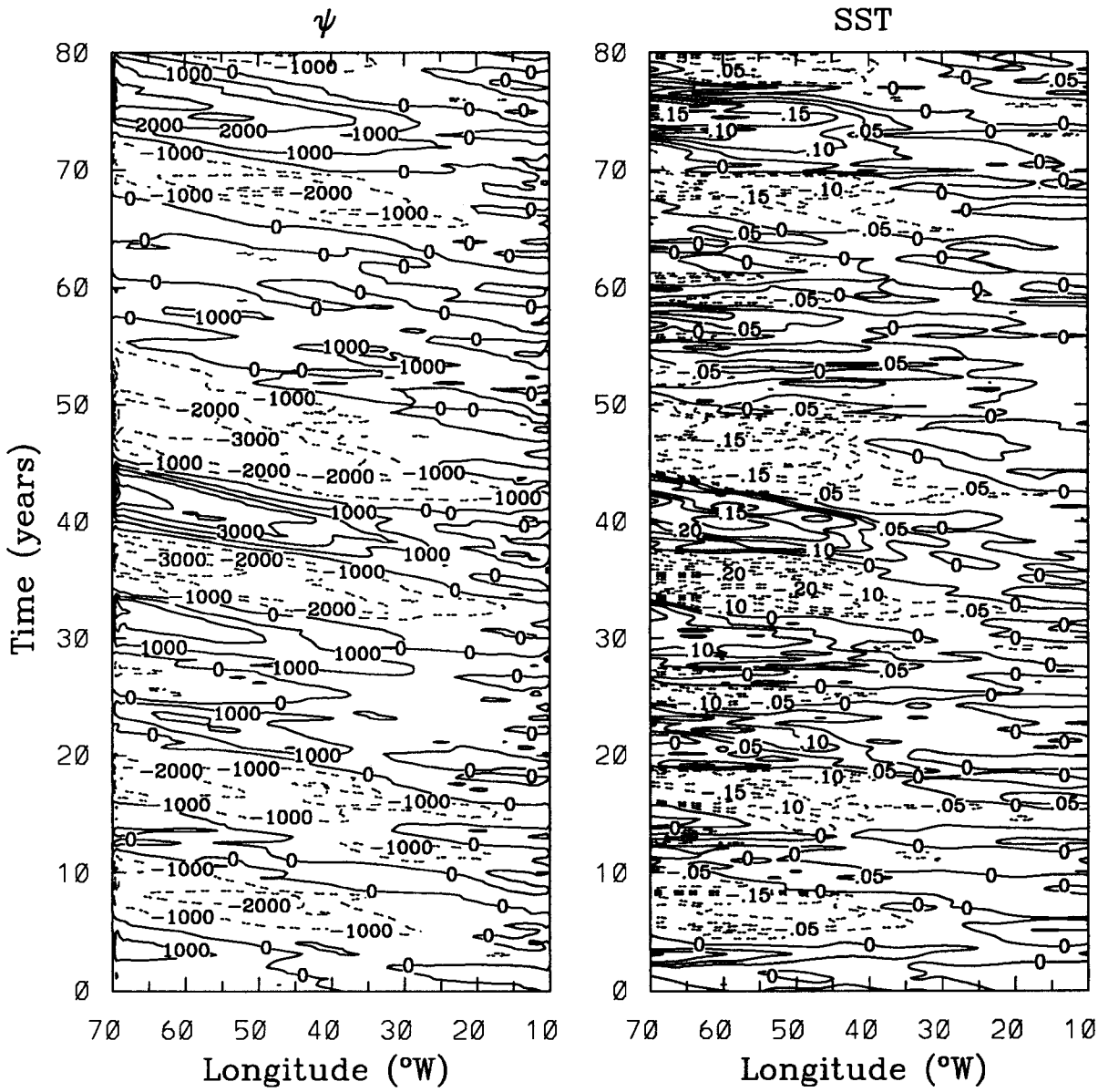

FIG. 6. Time–longitude plot of anomalies at 50°N for the coupled run ($\mu = 1$) over the North Atlantic. (a) Geostrophic streamfunction (contour interval 1000 $m^2 s^{-1}$); (b) SST anomaly (contour interval 0.05 K).

To examine the effect of coupling, we run the model without SST dependent noise (that is, uncoupled integration with $\mu = 0$). EOF 1 and EOF 2 of SST anomalies account for 30% and 23% of the total variance (Figs. 9a,c), respectively. These two EOFs share qualitative features with their counterparts from the coupled case but exhibit significant differences. For instance, EOF 1 of the uncoupled case has more of a monopole pattern. EOF 1 and EOF 2 of streamfunction account for 60% and 29% of the total variance (Figs. 9b,d), respectively, and have notable similarities to the corresponding EOFs in the coupled case.

Figure 10 shows power spectra of the leading EOFs based on three 1000-yr uncoupled integrations. The power spectrum is basically red for EOF 1 of geostrophic streamfunction and has a peak weaker than the coupled case for the EOF 2 (Fig. 10a). The period of this peak is approximately 11 yr. The period of the power spectral peak for SST anomalies is about 16 years for EOF 1 and 11 yr for EOF 2 (Fig. 10b). However, these peaks are less distinct than that of the coupled case. The correlations among the principal components of these EOFs are also symptomatic of the weaker distinction between the interdecadal oscillation and noise

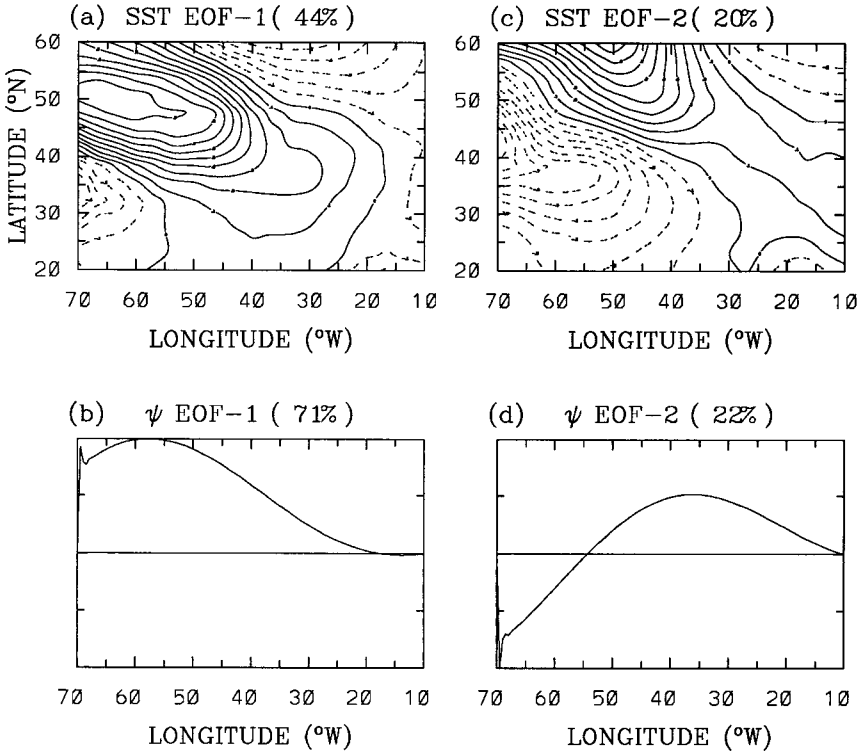

FIG. 7. Leading EOFs over North Atlantic based on a 1000-yr coupled run with additive and SST dependent noise atmosphere. The number in brackets at the top of each figure is the percentage of variance explained by the mode. (a) EOF 1 of SST anomalies, (b) EOF 1 of geostrophic streamfunction, (c) EOF 2 of SST anomalies, and (d) EOF 2 of geostrophic streamfunction.

background. For instance, the correlation of SST-EOF 1 with ψ-EOF 1 and SST-EOF 2 with ψ-EOF 2 are 0.45 and 0.5, respectively.

Due to uncertainties in the estimation of the standard deviation of additive heat flux forcing, we run the model with this variable ranging between 5 and 30 W m^{-2}. For the coupled run with large heat flux noise, the spatial pattern of EOF 1 of SST anomalies (Fig. 11a) is very similar to the nonlocal heat flux feedback pattern (Fig. 2b, or see Fig. 1b in Weng and Neelin 1998). This mode accounts for 75% of the variance of SST anomalies over the domain. No power-spectral peak is found for this mode (solid line in Fig. 11c) consistent with a decaying SST mode excited by noise, exactly as in the Hasselmann (1976) hypothesis. The spectrum is flat on long timescales compared to the decay time associated with negative feedbacks in heat flux; for short timescales, the spectrum is red. EOF 2 and EOF 3 of SST anomalies (figure not shown) and their power spectra (Fig. 11c) are similar to the EOF 1 and EOF 2 of the coupled case shown in Figs. 7 and 8 except that these two only account for total of 17% of the variance. The leading two EOFs of streamfunction (figure not shown) and their power spectra (Fig. 11b) are similar to the coupled case given above (see Figs. 7, 8). When uncoupled, the spatial patterns of the leading EOFs (not shown) are basically similar to the corresponding coupled case. The percentage of the variance explained by EOF 1 of SST is 88% and by both EOFs 2 and 3 of SST are 7%. The main difference is that in the uncoupled case, the power spectrum (Fig. 12) is basically red for EOF 1 of streamfunction and has a peak weaker than the corresponding coupled case for the EOF 2 of streamfunction and EOFs 2 and 3 of SST anomalies.

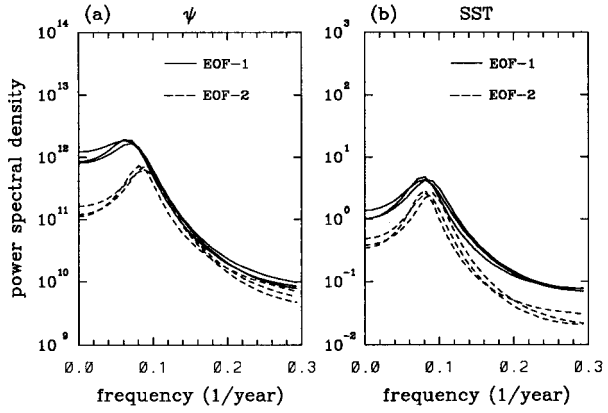

FIG. 8. The power spectral density of leading EOFs over North Atlantic based on three 1000-yr coupled runs. (a) For geostrophic streamfunction and (b) for SST.

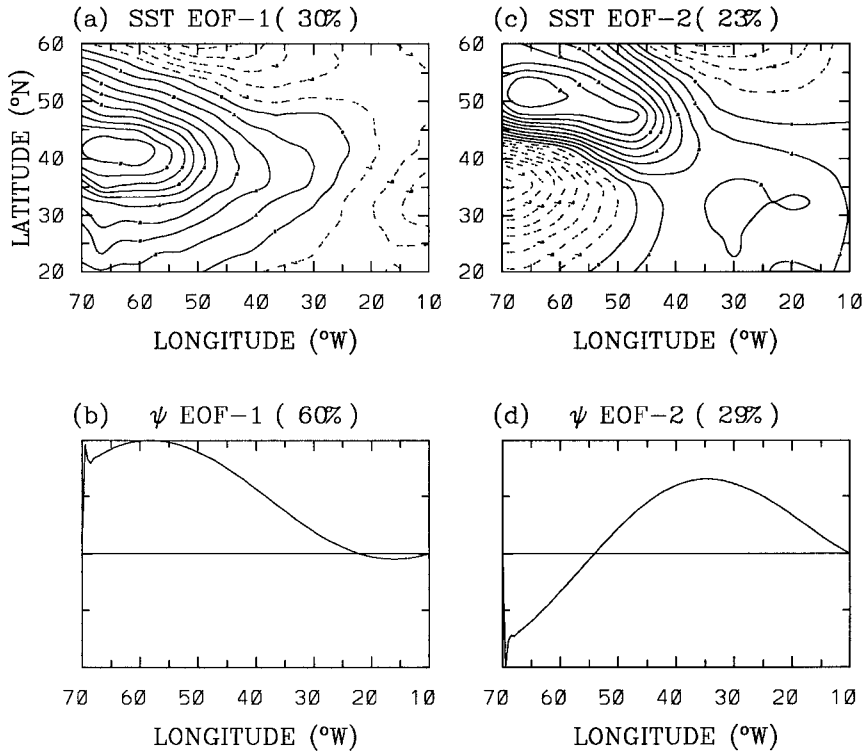

FIG. 9. Leading EOFs over North Atlantic based on a 1000-yr uncoupled run (with additive noise only). The number in brackets at the top of each figure is the percentage of variance explained by the mode. (a) EOF 1 of SST anomalies, (b) EOF 1 of geostrophic streamfunction, (c) EOF 2 of SST anomalies, and (d) EOF 2 of geostrophic streamfunction.

b. North Pacific

We test the case over the North Pacific with the basic fields estimated from Lau and Nath (1990). For the coupled integration, EOF 1 of SST anomalies (Fig. 13a) accounts for 40% of the total variance and has a spatial pattern similar to the heat flux feedback pattern shown in Fig. 4b because this pattern has been used in the additive noise. The power spectrum of this mode (solid line in Fig. 14b) is quite flat at low frequencies, indicating the role of heat flux forcing. EOF 2 and EOF 3 of SST anomalies account for 16% and 9% of total variance, respectively, and have a large-scale north–south dipole pattern (Figs. 13b,d). Their associated power spectral peaks are at 17 and 14 yr, respectively (Fig. 14b). EOF 1 and EOF 2 of streamfunction account for 50% and 38% of total variance, respectively, and have a smooth large-scale pattern that decays slowly toward the east (Figs. 13c,e). The leading EOFs of streamfunction have a power-spectral peak at periods of 25 and 17 yr (Fig. 14a). These features are similar to the coupled case in the North Atlantic with large heat flux standard deviations (i.e., $s_{a1}^{Q} = 30$ and $s_{m1}^{Q} = 5$ W m^{-2}) except that spatial scale for both anomalies is larger and the periods are longer. Correlations among principal components are 0.69 between SST-EOF 3 and ψ-EOF 1 and 0.79 between SST-EOF 2 and ψ-EOF 2.

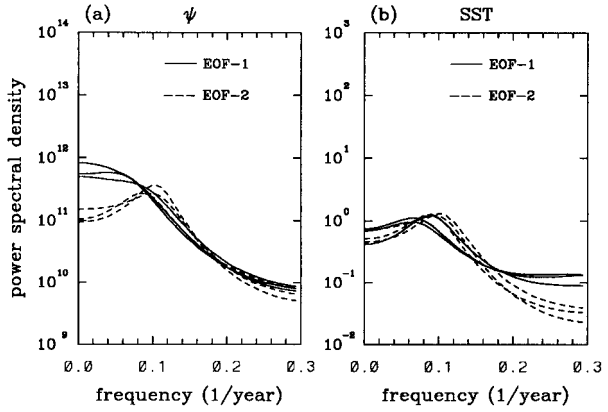

FIG. 10. The power spectral density of leading EOFs over the North Atlantic based on three 1000-yr uncoupled runs. (a) For geostrophic streamfunction and (b) for SST.

In the comparable uncoupled integration (Figs. 15 and 16), similar results are obtained. The main difference is that the percentage of the variance explained by EOF 1 of SST increases to 54% of the total variance (Fig. 15a). Power-spectral peak of the leading two EOFs of streamfunction and EOF 2 and 3 of SST anomalies has similar period (Fig. 16) as in the coupled case (Fig. 14) although the peak is slightly less distinct. Thus, unlike the Atlantic case above, power-spectral peaks still occur

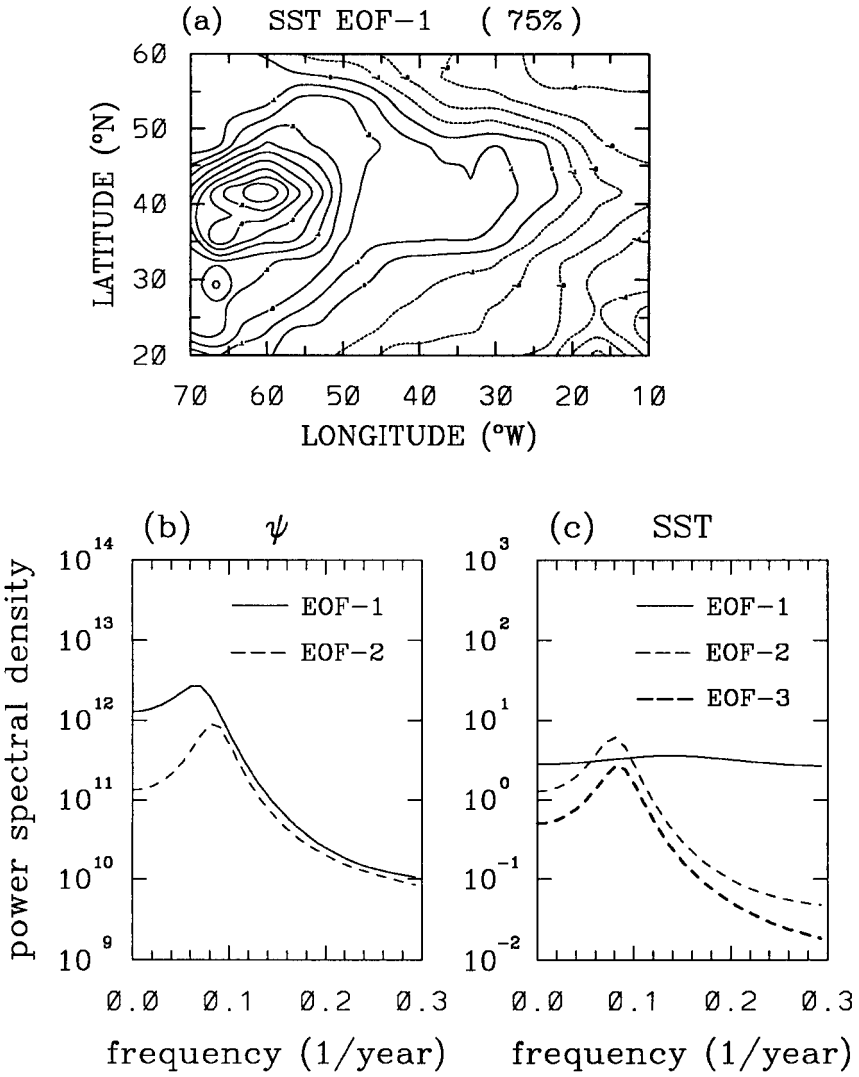

FIG. 11. (a) The leading EOF of SST anomalies, (b) the power spectra of leading EOFs of streamfunction, and (c) the power spectra of leading EOFs of SST over the North Atlantic based on a 1000-yr coupled run with $s_{a1}^{Q} = 30$ W m^{-2} and $s_{m1}^{Q} = 5$ W m^{-2}.

in SST and streamfunction for the *uncoupled* case (Fig. 16), as well as the coupled case. Clearly we need to explain a timescale selection mechanism that can operate separately for coupled and uncoupled cases.

We also test the case over the North Pacific with the feedback fields estimated from Latif and Barnett (1994). Due to their large positive heat flux feedback and large wind stress feedback, the SST anomalies increase exponentially with time in this linear model. While instability through ocean–atmosphere interaction could in theory be a potential source of interdecadal variability, and would equilibrate to finite amplitude in a nonlinear model, there are several reasons for studying a stabilized version of this case. First, there is some doubt that the feedbacks in the real system are as large as apparently occur in the case we take from Latif and Barnett (1994). For a 1°C SST anomaly, maximum magnitudes are over 1 dyn cm^{-2}, which is comparable to the climatological wind stress, and over 100 W m^{-2} net heat flux. The feedbacks they show are for a January case, which we apply through the year. Second, the interdecadal mode is actually stable (as shown in Weng 1997). The instability is due to an SST mode, which is nonoscillatory. As discussed in Neelin and Dijkstra (1995), such instabilities are typically caused by flux correction. We therefore seek a modification that will stabilize the SST mode and permit us to study the period and spatial structure of the interdecadal mode. We modify their case using magnitudes of heat flux and wind stress feedbacks reduced to the same magnitudes as estimated in the Lau and Nath (1990) case but keeping the Latif and Barnett spatial feedback patterns and their positive heat flux

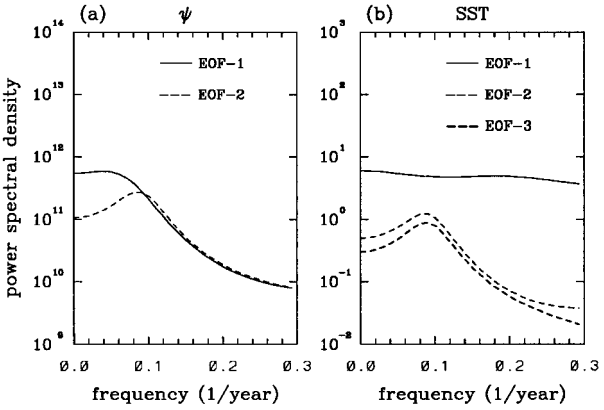

FIG. 12. The power spectra of leading EOFs over the North Atlantic based on a 1000-yr uncoupled run with $s^Q_{a1} = 30$ W m^{-2}. (a) For geostrophic streamfunction and (b) for SST.

feedback. We refer to this as a ''Latif and Barnett–like'' case. For both the coupled and uncoupled cases, the basic features of the leading two EOFs of streamfunction and SST anomalies (figure not shown) are similar to the Atlantic case with small heat flux noise (i.e., $s^Q_{a1} = 5$ W m^{-2}) except the zonal length scale is larger. Similarly, the percentage of the variance explained by both EOF 1 and EOF 2 in the uncoupled case is less than that in the coupled case. For the coupled case, the periods of the power spectral peaks are 25 and 17 yr for EOF 1 and EOF 2 of streamfunction, respectively, and 17 and 12 yr for EOF 1 and EOF 2 of SST anomalies, respectively. The uncoupled case has similar power-spectral peaks, but they are slightly less distinct. In the coupled case, the interdecadal oscillations can be seen clearly from the time–longitude plot of geostrophic streamfunction and the SST anomalies at 50°N (Fig. 17). The geostrophic streamfunction shows characteristics of westward propagation, while in SST this propagation is less clear, probably due to effects of heat flux noise.

Overall, these results indicate that the uncoupled system can give coherent spatial patterns in the oceanic response due to effects of the basic state and large-scale atmospheric stochastic forcing. The uncoupled ocean can even exhibit weak spectral peaks when forced by spatially coherent, temporally white (on timescales longer than a week) atmospheric noise. However, coupling of the SST pattern to a large-scale atmospheric pattern—even if only by a small effect of SST on the atmospheric PDF—can have a significant effect on oceanic spatial pattern and timescales.

6. Deterministic coupling cases

a. Deterministic coupling as a limit of SST dependent noise

In general, multiplicative noise effects can be exotic (Horsthemke and Lefever 1984, and references therein). We investigate cases with various standard deviations of the multiplicative noise components ranging between 0 and twice the standard deviation of the respective additive noise components. When standard deviations of additive and multiplicative wind stress are 0.4 and 0.8 dyn cm^{-2} (the North Atlantic case), respectively, the PDF of the total wind stress has a standard deviation about 0.89 dyn cm^{-2} and the mean value is slightly greater than zero. As the standard deviation of multiplicative noise approaches zero, the atmospheric wind stress reduces to a deterministic feedback plus additive noise. The PDF of wind stress for this case has the same standard deviation as that of the additive noise but is shifted by a mean value, which depends on T_1. Similar remarks apply to the heat flux forcing as the standard deviation of multiplicative noise approaches zero, except that the PDF shift is larger relative to the additive noise standard deviation.

We use a time-integration method to investigate coupled cases with s^τ_{m1} ranging between 0 and $2s^\tau_{a1}$ ($=0.8$ dyn cm^{-2} over the North Atlantic) and s^Q_{m1} ranging between 0 and $2s^Q_{a1}$ ($=10$ W m^{-2}). Nondimensionally, the upper end of this range is $\tilde{s}^\tau_{m1} = 8$ and $\tilde{s}^Q_{m1} = 1$, respectively. All other parameters and fields are as in the coupled case in the previous section. Here we refer to the North Atlantic case but similar behavior is obtained for the Pacific case. Spatial patterns of EOF 1 and EOF 2 of streamfunction and SST anomalies are very similar to the coupled case in the North Atlantic (Fig. 7) shown in section 5 for all values of s^τ_{m1} and s^Q_{m1} in the ranges given above. When standard deviations of multiplicative noise components are twice as large as that of the additive noise components, the total percentage of the variance explained by EOF 1 and EOF 2 is 68% for SST anomalies and 95% for the geostrophic streamfunction (figure not shown). As standard deviations of multiplicative noise components decrease, the percentage of explained variance also decreases, but the period peak is not very sensitive to the standard deviation of the multiplicative noise. Figure 18 gives the power spectra of the leading EOFs of streamfunction and SST anomalies based on two 1000-yr coupled integrations, one with $s^\tau_{m1} = 0.8$ dyn cm^{-2} and $s^Q_{m1} = 10$ W m^{-2}, and the other one with $s^\tau_{m1} = s^Q_{m1} = 0$. The lines with higher power correspond to the first case, since the larger atmospheric variability tends to excite larger response. Aside from this, the shape of the power spectra is very similar. Considering that the standard deviation of the wind stress multiplicative noise is eight times as large as the deterministic feedback, this similarity is quite remarkable. This occurs because the ocean characteristic response time is sufficiently long to integrate over much of the random variability in the feedback, and thus responds largely to the mean feedback.

Based on this, we can reduce the atmospheric model to the deterministic coupling plus the additive noise [Eqs. (4.4) and (4.5)] to study the simplified system. With atmospheric additive forcing given as before but with fixed spatial patterns, we can solve the power spec-

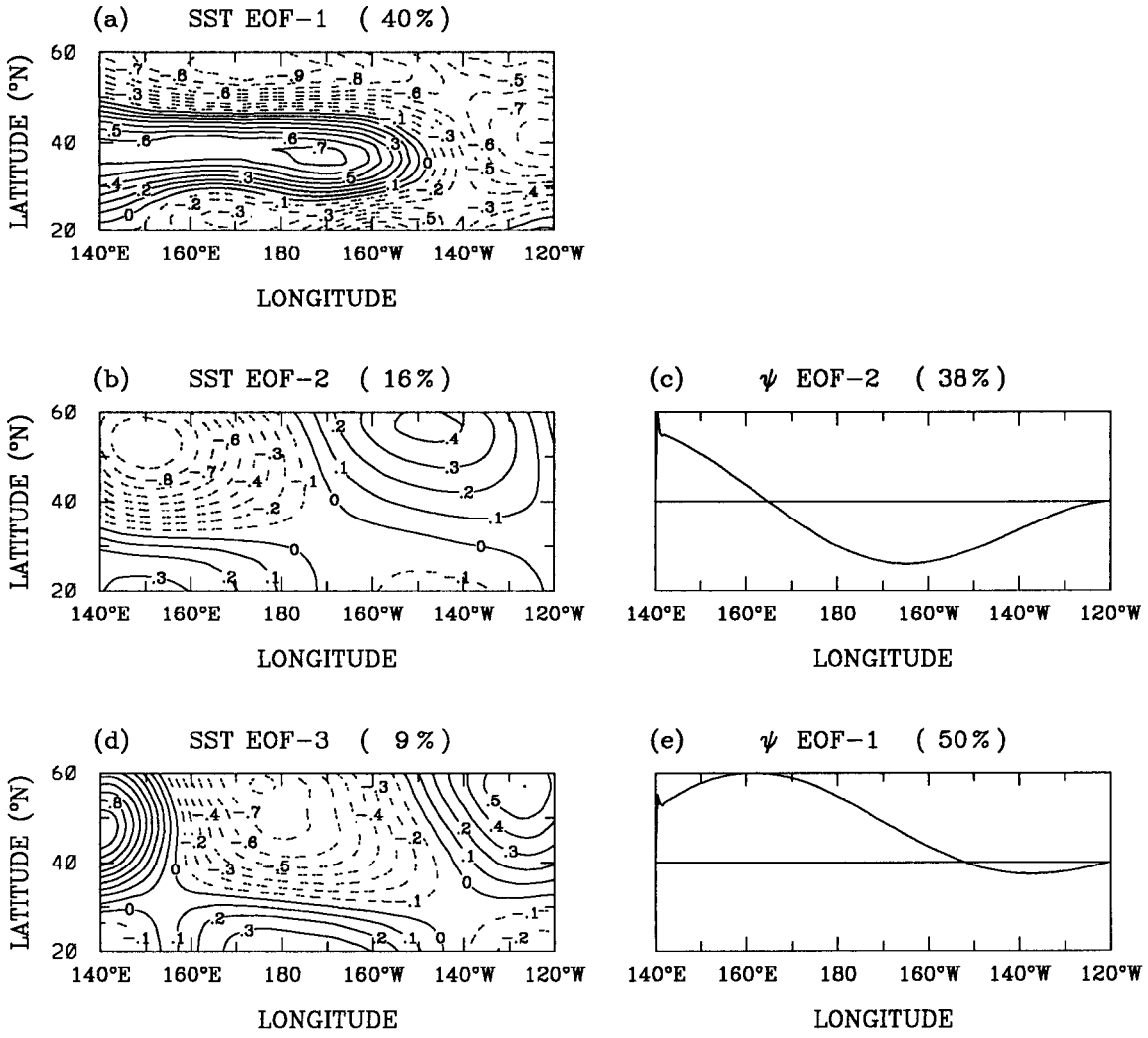

FIG. 13. Leading EOFs over the North Pacific based on a 1000-yr coupled run with additive and SST dependent noise atmosphere. The number in brackets at the top of each figure is the percentage of variance explained by the mode. (a) EOF 1 of SST anomalies, (b) EOF 2 of SST anomalies, (c) EOF 2 of geostrophic streamfunction, (d) EOF 3 of SST anomalies, and (e) EOF 1 of geostrophic streamfunction. The ψ-EOFs are ordered to appear beside the SST-EOF with which they are most strongly correlated.

trum either numerically (see appendix A) or near-analytically (see appendix B) using Fourier transformed equations. This avoids dependence on MEM order used for power-spectral analysis of the time series and makes the link between time-stepped and near-analytic results.

b. Near-analytic solutions

In Weng and Neelin (1998), we showed the power-spectral density in the North Atlantic for a simple case when additive atmospheric wind stress and heat flux forcing have the same spatial forms as the corresponding feedback patterns. In order to see the relative role of wind stress and heat flux, we examine a case similar to that given in Weng and Neelin (1998) but excluding heat flux feedback and noise (Fig. 19). As the coupling coefficient increases, a spectral peak for each variable starts to rise and is quite distinct when coupling coefficient is at the standard value ($\mu = 1$). The period of the spectral peaks is 17 yr (Fig. 19d). These features are similar to the case with heat flux included, indicating the important role of wind stress feedback in the interdecadal mode.

Figure 20 is similar to Fig. 19 except for the North Pacific case with the SST basis function and the atmospheric feedback patterns estimated based on Lau and Nath (1990). For the case shown, the spatial form of heat flux forcing is the same as the nonlocal heat flux feedback. The wavelength and phase of the zonal component of wind stress forcing are 13 600 km and π, respectively. When uncoupled ($\mu = 0$), there is a power-spectral peak at a period of 31 yr for geostrophic stream-

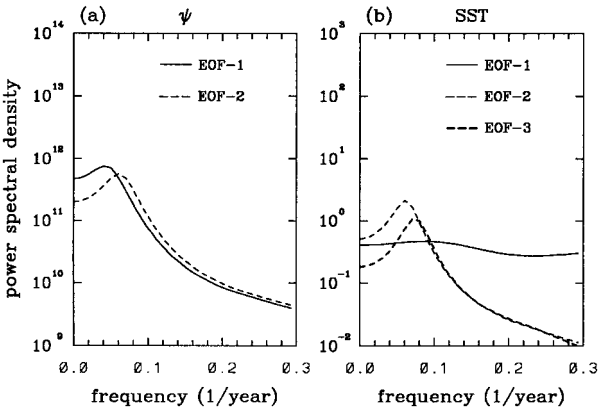

FIG. 14. The power spectral density of the leading EOFs for the coupled Pacific case given in Fig. 13. (a) For geostrophic streamfunction and (b) for SST.

function and 18 yr for SST. As μ increases, the spectral peaks become more distinct. When μ increases to the standard coupling coefficient ($\mu = 1$), the period of the peak is 25 yr for geostrophic streamfunction and 21 yr for SST anomalies.

This result is generally similar to the numerical results given in section 5 although the solution methods do lead to some differences in the period of spectral peaks.

c. *Effects of feedback pattern and distance from the western boundary*

In this subsection, we analyze the coupled model with an idealized form of the wind stress feedback to investigate the propagation of information toward the western boundary, and effects on period. We assume $J = 1$ and modify τ_{s1} and τ_{a1} in Eqs. (4.4) and (4.5) to the form

$$\tau_{s1} = \tau_{a1} = \begin{cases} -1 & \text{if } x_1 \le x \le x_2, \\ 0 & \text{otherwise,} \end{cases} \qquad (6.1)$$

where $0 \le x_1 \le x_2 \le L_x$ and L_x is the width of the ocean basin ($x = 0$ and $x = L_x$ are at western and eastern boundaries, respectively). The spatial form of Q_{a1} is either zero or is the same as the atmospheric heat flux feedback pattern Q_{s1}.

The power spectra of geostrophic streamfunction and SST anomalies for various wind stress forms over the North Atlantic (coupled) are given in Fig. 21. In the case shown, Q_{a1} has the same spatial form as the heat flux feedback pattern. For zonal wind stress between 45° and 65°W and zero elsewhere (Fig. 21a), only a very weak power-spectral peak with period around 9 yr is seen. In this case, the western edge of the wind stress, x_1, is 5° away from the western boundary. When the western edge of the wind stress is 15°, 25°, and 35° of longitude away from the western boundary, with the same longitudinal extent, the period of the peaks for both geostrophic streamfunction and SST anomalies are about 11, 16, and 25 yr, respectively (see Figs. 21b,c,d).

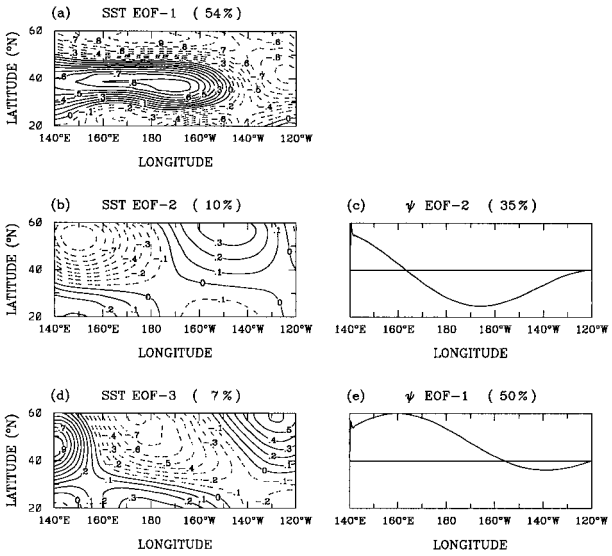

FIG. 15. Leading EOFs over the North Pacific based on a 1000-yr uncoupled run with additive noise atmosphere. The number in brackets at the top of each figure is the percentage of variance explained by the mode. (a) EOF 1 of SST anomalies, (b) EOF 2 of SST anomalies, (c) EOF 2 of geostrophic streamfunction, (d) EOF 3 of SST anomalies, and (e) EOF 1 of geostrophic streamfunction. The ψ-EOFs are ordered to appear beside the SST-EOF with which they are most strongly correlated.

That is, the period of the power-spectral peak increases as the zonal wind stress moves to the east. This is because the dominant timescale mechanism is associated with long Rossby waves, which propagate to the west (in the sense of group velocity). If this wave is excited far from the western boundary, it takes more time for the information to propagate westward, tending to favor a longer period. However, the period does not increase linearly with the distance between the western boundary and the wind stress. We have also tested the case when there is no heat flux ($Q_{s1} = Q_{a1} = 0$), with results close to the case shown in Fig. 21.

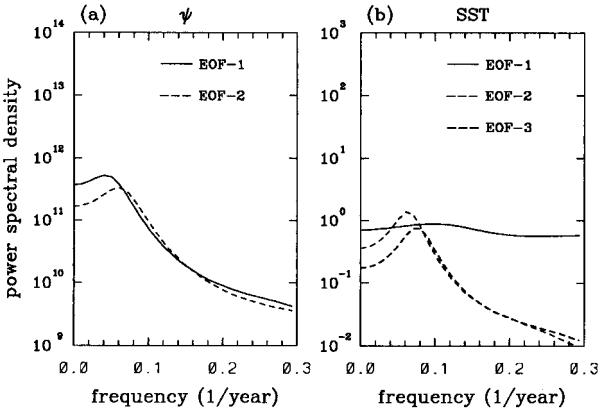

FIG. 16. The power spectral density of the leading EOFs for the uncoupled Pacific case given in Fig. 15. (a) For geostrophic streamfunction and (b) for SST.

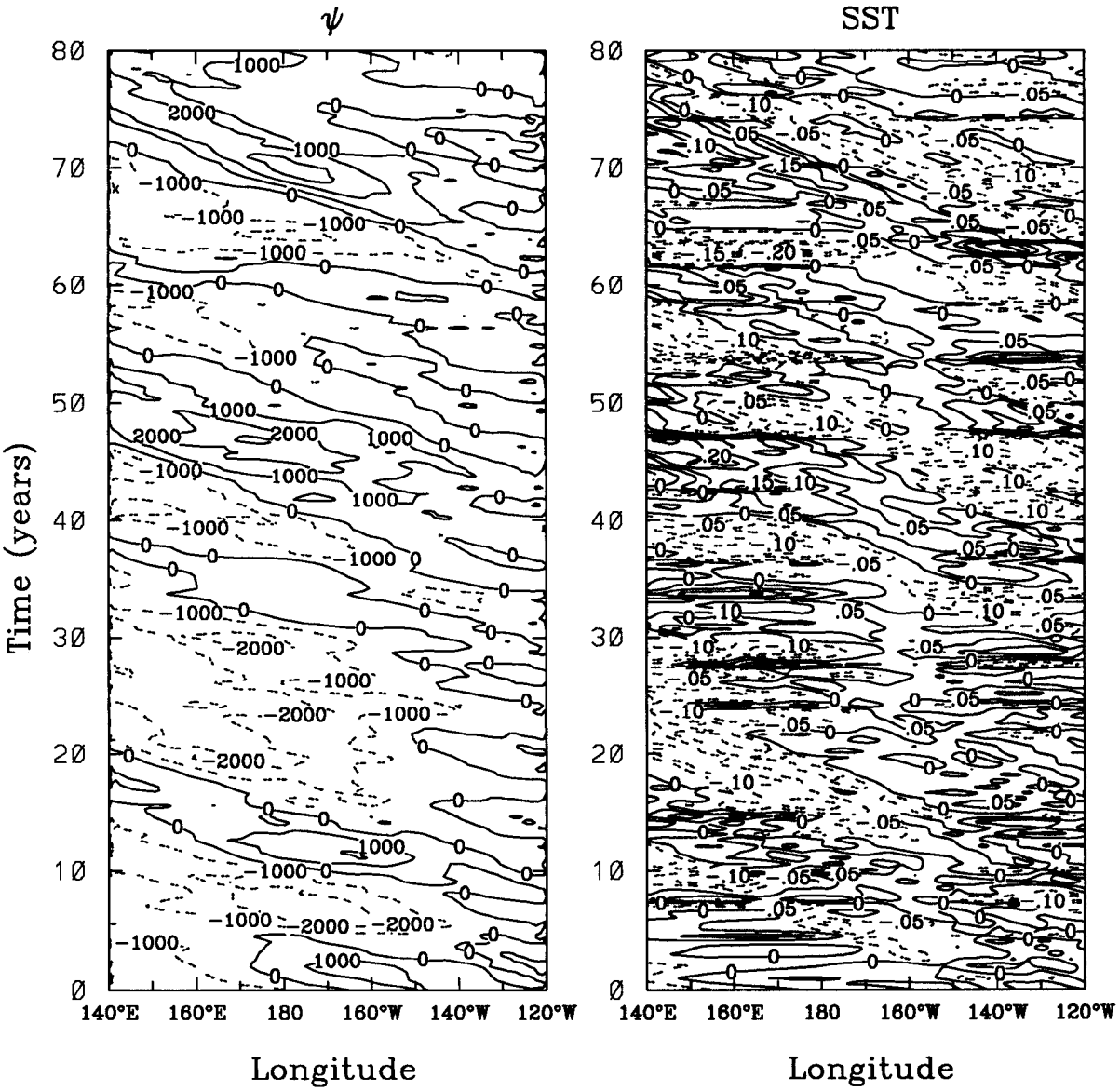

FIG. 17. Time–longitude plot of anomalies at 50°N for the coupled run ($\mu = 1$) over the North Pacific for the Latif and Barnett–like case. (a) Geostrophic streamfunction (contour interval 1000 $m^2\ s^{-1}$); (b) SST anomaly (contour interval 0.05 K).

7. Discussion and conclusions

A simple ocean–atmosphere coupled model is used to study potential coupled feedback mechanisms at midlatitudes and their consequences. Due to the large internal variability of the atmosphere at midlatitudes, response to SST anomalies is represented as a stochastic process. Coupling is postulated to occur through the influence of SST on the probability density function of the atmospheric noise. We represent this simply by an additive noise process, representing the component of atmospheric internal variability independent of SST, and an SST dependent noise process, representing the atmospheric response to the ocean. The SST dependent noise is approximated by a large-scale spatial pattern associated with a random variable whose probability density function ensemble mean and variance depend on SST. Seasonal dependence is omitted here.

We investigate the role of this SST dependent noise coupling by running the model with SST dependent noise included (coupled hereafter) or without it, that is, with purely additive noise (uncoupled). In the North Atlantic, the uncoupled integration has leading EOFs of geostrophic streamfunction with smooth large-scale spatial patterns that decay eastward. The power spectra is basically red for EOF 1 and has a weak peak at interdecadal timescale for EOF 2. The leading EOFs of SST

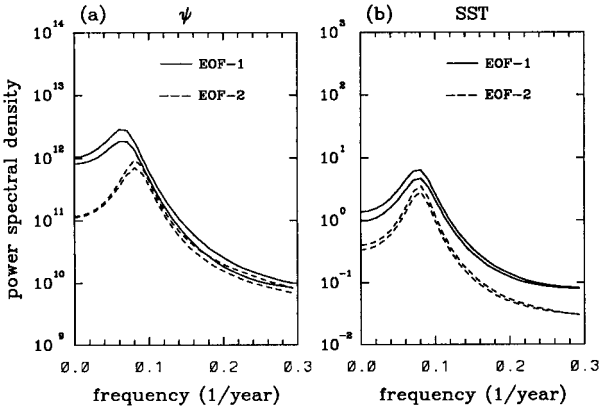

FIG. 18. The power-spectral density of leading EOFs over the North Atlantic based on two 1000-yr coupled runs. The lines with more power are for the case when $s^{\tau}_{m1} = 0.8$ dyn cm^{-2} and $s^{Q}_{m1} = 10$ W m^{-2}. The lines with less power are for the case when $s^{\tau}_{m1} = s^{Q}_{m1} = 0$. (a) For geostrophic streamfunction and (b) for SST anomalies.

exhibit sensitivity to the standard deviation of stochastic heat flux forcing. When heat flux noise is small, the leading EOFs of SST have a large-scale north–south dipole pattern associated with the leading EOFs of streamfunction, indicating the dominant role of wind stress forcing in generating the SST pattern. The power spectra of the leading EOFs show a weak peak at periods of interdecadal timescale. When heat flux noise is large, EOF 1 of SST has a spatial pattern closely related to the heat flux forcing, indicating the role of heat flux. The power spectrum of this mode is flat as in the Hasselmann (1976) hypothesis for timescales longer than heat flux negative feedback timescales. For the coupled

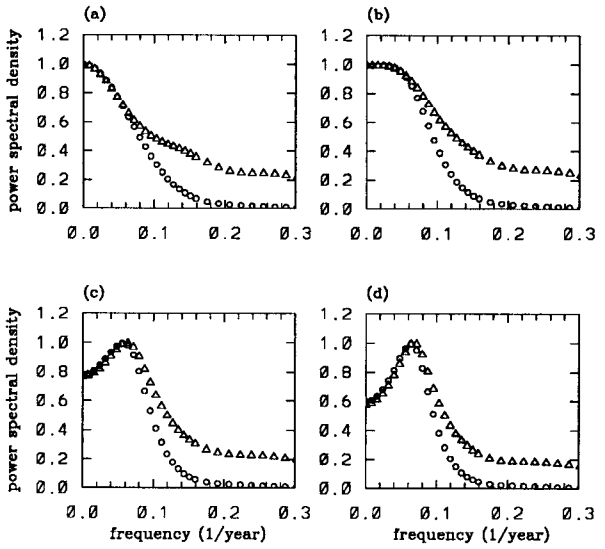

FIG. 19. The power-spectral density of geostrophic streamfunction (open circles) and SST anomaly (open triangles) in the North Atlantic ocean (summed over all points) for a case with deterministic wind stress feedback and additive wind stress noise. (a) For $\mu = 0.1$; (b) for $\mu = 0.3$; (c) for $\mu = 0.7$; and (d) for standard coupling, $\mu = 1$.

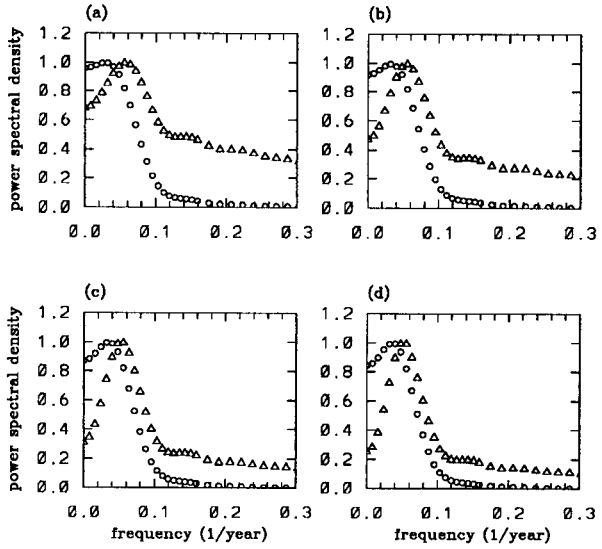

FIG. 20. The power-spectral density of geostrophic streamfunction (open circles) and SST anomaly (open triangles) in the North Pacific ocean (summed over all points) for a case with deterministic wind stress and heat flux feedbacks and additive noise. (a) For $\mu = 0.0$; (b) for $\mu = 0.3$; (c) for $\mu = 0.7$; and (d) for standard coupling, $\mu = 1$.

case with SST dependent noise included, the spatial patterns of the EOFs of streamfunction and SST anomalies are generally similar to that of the corresponding uncoupled case. The main difference is that for many cases there is an obvious rise of a power-spectral peak at interdecadal periods for the leading EOFs associated with the interdecadal mode.

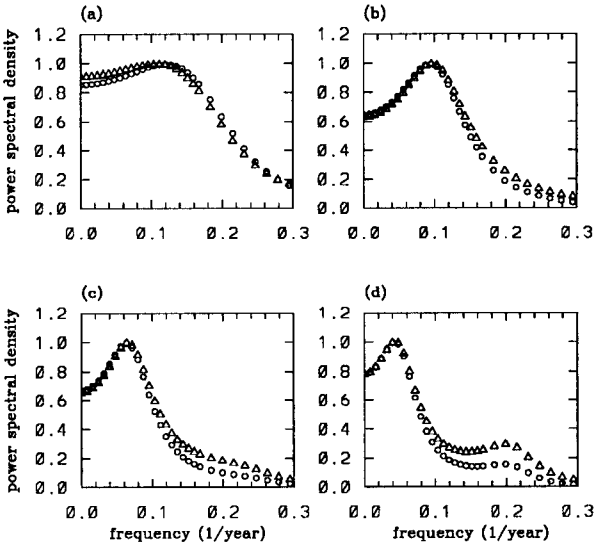

FIG. 21. Power spectra of geostrophic streamfunction (open circles) and SST anomaly (open triangles) in the North Atlantic Ocean (summed over all points) with wind stress feedback and additive wind stress noise constant between longitudes x_1 and x_2, zero elsewhere: (a) $x_1 = 65°$W, $x_2 = 45°$W; (b) $x_1 = 55°$W, $x_2 = 35°$W; (c) $x_1 = 45°$W, $x_2 = 25°$W; and (d) $x_1 = 35°$W, $x_2 = 15°$W.

In the North Pacific, we tested two cases intended to mimic Lau and Nath (1990) and Latif and Barnett (1994), respectively. Behavior is qualitatively similar to the North Atlantic case with large and small heat flux noise, respectively. The most robust difference from the Atlantic case is that both cases have longer zonal length scales in the leading EOFs of the interdecadal modes and correspondingly longer periods. In both oceans, their spatial scales are similar to the scales given by the atmosphere over the domain, that is, the atmosphere plays a dominant role in selecting the length scale of the leading ocean modes in this system. We do find a case where the Latif and Barnett (1994) feedbacks give an unstable nonoscillatory SST mode, which is probably spurious. Even for the large feedbacks in their case, the interdecadal mode is stable. We hypothesize that, in general, stable modes maintained by atmospheric noise are the most likely prototype for midlatitude interdecadal variability.

Because the standard deviation of multiplicative noise, s_{m1}, is poorly constrained by data, we examine cases with s_{m1} ranging between 0 and twice the standard deviation of the additive noise (for both oceans). The case where $s_{m1} = 0$ corresponds to a deterministic feedback on SST (combined with the additive noise). Changes in s_{m1} primarily affect the percentage of variance explained by the leading EOFs and the level of their power spectra. The value of s_{m1} is not crucial in selecting time or spatial scales of the leading modes because in our linear model, the ocean tends to integrate multiplicative noise. The ocean timescales are sufficiently long that the integrated effect of the stochastic atmospheric response on the ocean is similar to that of a deterministic atmospheric feedback.

We can thus usefully study an atmospheric component consisting of additive stochastic forcing plus deterministic feedbacks. A near-analytic solution of the power spectral density for this simplified system shows that although a weak peak at interdecadal timescale can appear in some uncoupled cases, coupling can enhance the peak. The analysis of cases with and without heat flux feedback indicates that the interdecadal power spectral peak is due to atmospheric wind stress. For the standard coupling case, this solution gives a period of 17 yr for both SST and streamfunction in the North Atlantic and 21 yr for SST and 25 yr for streamfunction in the North Pacific. These periods differ slightly from the periods of the leading EOFs obtained from the time-integration method. It is worth noting the imperfect match of apparent peaks in SST and streamfunction as a caution to interpreting results in observations or more complex models. Here we can demonstrate that we have a coupled mode with a well-defined period and yet even with long time series or analytical spectra, the presence of other (red) types of variability appears to affect the position of the spectral peak differently in different fields. Although these values are sensitive to the methods used and some parameters, these periods can roughly be compared to GCM results. Latif and Barnett (1994, 1996) and Robertson (1996) find timescales on the order of 20 yr in the North Pacific, while Grötzner et al. (1998) note an 18-yr timescale in the North Atlantic in two MPIM coupled models, and Selten et al. (1998) find 16–18 yr in their coupled model. When considering this mechanism compared to observations, a caveat must be borne in mind that observed oceanic baroclinic Rossby wave speeds are significantly faster than standard theory (Chelton and Schlax 1996). Thus the periods may tend to be somewhat shorter than those obtained here. For instance, the spectral peak noted in EOFs of SST and surface air temperature in the Atlantic by Deser and Blackmon (1993) is around 12 yr. However, we emphasize here the overall physical mechanism rather than the precise period. We also note that for current observational time series, the case for distinct spectral peaks is far from clear. The mechanism proposed here suggests preferred timescales and spatial patterns might be found within the red noise background variance, but we do not expect such peaks to stand out strongly.

The time–longitude plots (from the time integrated model version) have signatures of westward propagation of geostrophic streamfunction in the interdecadal mode for both basins. Although the time–longitude plot of SST anomalies shows a clear association with the streamfunction, westward propagation is less clear in SST. To investigate the information propagation, we test cases with the atmospheric feedback simplified to a zonally constant wind stress patch located at different longitudes in several experiments. The distance between the western boundary and the wind stress feedback region affects the period of the power-spectral peak. Larger distance tends to have longer period, consistent with Rossby wave propagation from the feedback region toward the west.

A schematic representation of the ocean–atmosphere feedback process is given in Fig. 22. This diagram highlights the important role of the atmosphere in setting the zonal length scale of the ocean and the oceanic Rossby wave dynamics in selecting the timescale as suggested by Weng and Neelin (1997). Part II of this paper (Weng and Neelin 1999) gives a more detailed investigation of the selection of a preferred time scale of the interdecadal modes by looking for a near-analytic solution of the eigenvalue problem of the coupled model. Although we have noted some complicated behavior of the spectral response of the coupled system in the text, a rule of thumb for preferred interdecadal time scales in the uncoupled and coupled cases, respectively, can be summarized as follows. In the uncoupled case, if there is a preferred length scale in the large-scale atmospheric stochastic forcing, oceanic Rossby waves will tend to be excited with this scale. These waves propagate to the west with group (and phase) velocity $c_{\text{Rossby}} \approx \beta\lambda^2$. Then the period is determined by L/c_{Rossby}, where L is the zonal length scale of the atmospheric forcing. Similar results are found by Jin (1997) from analysis in a simpler system and by Frankignoul et al. (1997) with L the basin scale for a case with zonally constant forcing. For typical large-scale

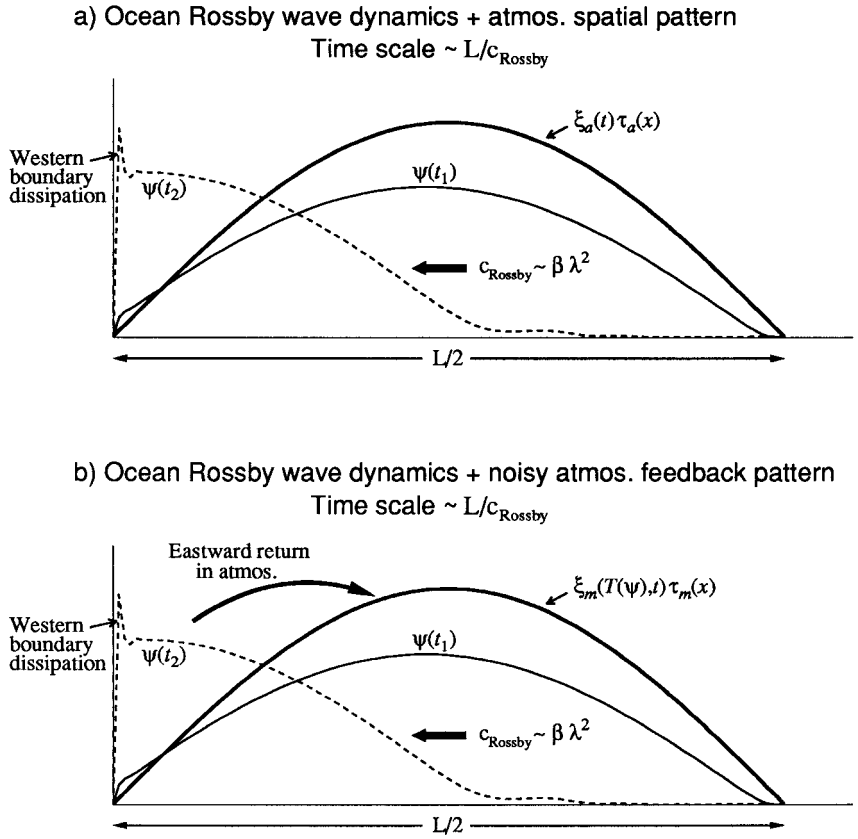

FIG. 22. Schematic diagram of mechanisms producing preferred timescales. (a) The uncoupled ocean case. Atmospheric additive stochastic forcing with a preferred spatial pattern, $\xi_a(t)\tau_a(x)$, tends to excite an oceanic Rossby wave whose geostrophic streamfunction ψ is shown at an early time t_1 and a later time t_2 after westward propagation with group velocity $c_{Rossby} \approx \beta\lambda^2$, where λ is the internal mode radius of deformation. Although the wave dies out at the western boundary, there is still a preferred timescale L/c_{Rossby}, where L is the atmospheric spatial scale, that can produce a weak spectral peak. (b) The coupled ocean–atmosphere case. A noisy SST dependent atmospheric feedback, $\xi_m(T(\psi), t)\tau_m(x)$, tends to excite an oceanic Rossby wave that likewise propagates westward at c_{Rossby}. SST anomalies produced by streamfunction anomalies ψ tend to reexcite the Rossby wave in the basin interior, so the spectral peak can be enhanced relative to the uncoupled case. The streamfunction ψ used in the diagram is the response to an impulse in time of wind stress, $\tau_a(x)$, shown for $t_1 = 5$ months and $t_2 = 4.5$ yr.

atmospheric forcing and oceanic Rossby deformation radius, these waves have periods of interdecadal timescale. In this uncoupled case, there is an underlying mathematical similarity to the ''advective ocean–atmosphere interaction'' mechanism proposed by Saravanan and McWilliams (1998) in which the speed of mean ocean currents provides a velocity scale for advection of SST, while the atmosphere sets the length scale. Here Rossby wave group velocity sets the velocity scale. The difference between wave dynamics and pure advection is most notable in the complex western boundary dynamics that enters here. Without an atmospheric feedback process (Fig. 22a), the long Rossby waves will die out when reaching the western boundary due to the dissipation there (combined with the slow eastward group velocity of reflected short Rossby waves).

For the coupled case (Fig. 22b), the SST anomalies generated by geostrophic current can feed back to the atmosphere. The atmosphere, in turn, brings some information back to the east and reexcites oceanic waves there. The essence of the timescale is, like the uncoupled case, given by long Rossby wave group velocity versus an atmospheric length scale, in this case the length scale of the feedback pattern. Even if the feedback is stochastic, as in the SST dependent noise case treated here, the return of some information to the central basin tends to reinforce the oscillation tendency and enhance the spectral peak.

This investigation suggests that atmospheric internal variability alone can give coherent spatial patterns and sometimes weak spectral peaks in the oceanic response due to effects of the basic state and large-scale atmospheric stochastic forcing. Even noisy atmospheric coupling due to slight change of the atmospheric PDF can

produce significant impact on spatial patterns of leading SST modes and make the power-spectral peaks more distinct relative to uncoupled ocean. Such changes in PDF will be challenging to diagnose from data. Large ensembles from AGCM experiments should help specify the PDF more accurately. While the role proposed here for coupled feedbacks in the midlatitude ocean–atmosphere system is subtle, it should be testable in more complex climate models.

Acknowledgments. This work was supported by National Science Foundation Grant ATM-9521389. NCAR Scientific Computing Division provided the computer resources. This work was motivated by discussions with Mojib Latif during a sabbatical (JDN) at MPIM in 1993. We wish to thank Drs. Michael Ghil, James C. McWilliams, Cecile Penland, and Andrew W. Robertson for their suggestions and comments.

APPENDIX A

Numerical Method

Fourier decomposing in time basis functions $e^{-i\omega t}$, where ω is the frequency, Eqs. (4.4) and (4.5) become

$$[-i\omega(\partial_x^2 - l^2 - \lambda^{-2}) + \beta\partial_x + \epsilon_c(\partial_x^2 - l^2) - \nu(\partial_x^2 - l^2)^2]\tilde{\psi}(x) = \frac{l}{\rho H}\left[\mu\tau_{s1}(x)\frac{\langle\theta_1\tilde{T}\rangle}{\langle\theta_1^2\rangle} + \sum_{j=1}^{J}\tau_{aj}(x)\tilde{\xi}_{aj}^{\tau}\right] \quad \text{(A.1)}$$

$$(-i\omega + \epsilon_T)\tilde{T}(x, y) = [l\cos(ly + \gamma)\partial_x\overline{T} - \sin(ly + \gamma)\partial_y\overline{T}\partial_x]\tilde{\psi}(x) + \frac{1}{f\rho H_1}\cos(ly + \gamma)\partial_y\overline{T}\left[\mu\tau_{s1}(x)\frac{\langle\theta_1\tilde{T}\rangle}{\langle\theta_1^2\rangle} + \sum_{j=1}^{J}\tau_{aj}(x)\tilde{\xi}_{aj}^{\tau}\right] + \frac{1}{c_w\rho H_1}\left[\mu Q_{s1}(x,y)\frac{\langle\theta_1\tilde{T}\rangle}{\langle\theta_1^2\rangle} + \sum_{j=1}^{J}Q_{aj}(x,y)\tilde{\xi}_{aj}^{Q}\right], \quad \text{(A.2)}$$

where $\tilde{\psi}$ and $\tilde{T}$ are the spectral density functions. The vector form of the above forced system is

$$(\mathbf{A} - i\omega\mathbf{B})\tilde{\mathbf{X}} = \sum_{j=1}^{J}\tilde{F}_j(\omega)\mathbf{f}_j, \quad \text{(A.3)}$$

where i is $\sqrt{-1}$. Here, $\tilde{\mathbf{X}}$ is the Fourier-transformed response eigenvector of ψ and T for a given frequency, $\tilde{F}_j$ represents the Fourier-transformed t structure of the jth forcing, and $\mathbf{f}_j$ denotes the jth spatial structure including both dynamic and thermodynamical sources. Here, $\mathbf{A}$ and $\mathbf{B}$ are the $I \times I$ square matrices with I dimensioned as the sum of grid points for both vorticity and SST equations. We use a resolution for the vorticity equation of 0.5° and for the SST equation of 3°.

Equation (A.3) can also be written as

$$\tilde{\mathbf{X}} = \sum_{j=1}^{J}\mathbf{H}_j(x, y, \omega)\tilde{F}_j(\omega), \quad \text{(A.4)}$$

where

$$H_{jl} = (\mathbf{A} - i\omega\mathbf{B})^{-1}f_{jl} \quad \text{(A.5)}$$

is the transfer function for a given variable and ω. Then the power-spectral density of the response, $S_{\tilde{\mathbf{X}}_l}$, to random forcing of input spectral density $S_{\tilde{F}}$, is

$$S_{\tilde{\mathbf{X}}_l} = \sum_{j=1}^{J}|H_{jl}|^2 S_{\tilde{F}}. \quad \text{(A.6)}$$

APPENDIX B

Analytic Method

If $\tau_{s1}(x) = \sum_{n=0}^{N}\tau_n\cos(k_n x + \alpha_n)$ and τ_{aj} has sinusoid form, Eq. (A.1) can be written as

$$[-i\omega(\partial_x^2 - l^2 - \lambda^{-2}) + \beta\partial_x + \epsilon_c(\partial_x^2 - l^2) - \nu(\partial_x^2 - l^2)^2]\tilde{\psi}(x) = \sum_{n=0}^{N+J}a_n\cos(k_n x + \alpha_n), \quad \text{(B.1)}$$

where

$$a_n = \frac{\mu l\tau_n\langle\theta_1\tilde{T}\rangle}{\rho H\langle\theta_1^2\rangle}, \quad \text{for } n = 0, \ldots, N; \quad \text{(B.2)}$$

$$a_n = \frac{l\tilde{\xi}_{an}^{\tau}}{\rho H}, \quad \text{for } n = N + 1, \ldots, N + J. \quad \text{(B.3)}$$

A particular solution of (B.1) is

$$\tilde{\psi}_P(x) = \sum_{n=0}^{N+J}\frac{a_n}{A_n^2 + \beta^2 k_n^2} \times [\beta k_n\sin(k_n x + \alpha_n) - A_n\cos(k_n x + \alpha_n)], \quad \text{(B.4)}$$

where

$$A_n = -i\omega(k_n^2 + l^2 + \lambda^{-2}) + \epsilon_c(k_n^2 + l^2) + \nu(k_n^2 + l^2)^2. \quad \text{(B.5)}$$

Then the solution of (B.1) can be written as

$$\tilde{\psi}(x) = \tilde{\psi}_P(x) + c_1 e^{r_1 x} + c_2 e^{r_2 x} + c_3 e^{r_3 x} + c_4 e^{r_4 x}, \quad \text{(B.6)}$$

where c_1, c_2, c_3, and c_4 are amplitudes determined by the boundary conditions (no flow and no slip). Here, r_1, r_2, r_3, and r_4 are four roots of the following equation:

$$\nu r^4 - (2\nu l^2 - i\omega + \epsilon_c)r^2 - \beta r - i\omega(l^2 + \lambda^{-2}) + \nu l^4 + \epsilon_c l^2 = 0. \quad \text{(B.7)}$$

By substituting $\tilde{\psi}(x)$ in (B.6) into Eq. (A.2) and taking the inner product of θ_1 with the equation over the basin, we can obtain $\langle\theta_1\tilde{T}\rangle$ from the resulting equation. Then

Fourier-transformed geostrophic streamfunction and SST anomalies can be obtained from (B.6) and (A.2), respectively, for various frequencies.

Due to the complexity of expression for the case $\nu \neq 0$, here we give the solution for a simple case when $\nu = 0$ and $\tau_{s1}(x) = \tau_A \cos(k_0 x + \alpha_0)$. In this case,

$$\tilde{\psi}(x, \omega) = \mu\tau_A\psi_0 \frac{\langle\theta_1\tilde{T}\rangle}{\langle\theta_1^2\rangle} + \sum_{j=1}^{J} \tilde{\xi}^{\tau}_{aj}(\omega)\psi_j, \tag{B.8}$$

$$\begin{aligned}\tilde{T}(x,y,\omega) = {} & (\epsilon_T - i\omega)^{-1}\frac{\mu\langle\theta_1\tilde{T}\rangle}{\langle\theta_1^2\rangle} \\ & \times \left[\tau_A\mathcal{L}(\psi_0) + \tau_A V_0 + \frac{Q_{s1}}{c_w\rho H_1}\right] \\ & + (\epsilon_T - i\omega)^{-1} \\ & \times \sum_{j=1}^{J}\left\{\tilde{\xi}^{\tau}_{aj}(\omega)[\mathcal{L}(\psi_j) + V_j] + \frac{\tilde{\xi}^{Q}_{aj}(\omega)Q_{aj}}{c_w\rho H_1}\right\},\end{aligned} \tag{B.9}$$

where

$$\langle\theta_1\tilde{T}\rangle = \frac{\displaystyle\sum_{j=1}^{J}\left\{\tilde{\xi}^{\tau}_{aj}(\omega)[\langle\theta_1\mathcal{L}(\psi_j)\rangle + \langle\theta_1 V_j\rangle] + \tilde{\xi}^{Q}_{aj}(\omega)\frac{\langle\theta_1 Q_{aj}\rangle}{c_w\rho H_1}\right\}}{\epsilon_T - i\omega - \dfrac{\mu}{\langle\theta_1^2\rangle}\left[\tau_A\langle\theta_1\mathcal{L}(\psi_0)\rangle + \tau_A\langle\theta_1 V_0\rangle + \dfrac{\langle\theta_1 Q_{s1}\rangle}{c_w\rho H_1}\right]}, \tag{B.10}$$

$$\mathcal{L} = l\cos(ly + \gamma)\partial_x\overline{T} - \sin(ly + \gamma)\partial_y\overline{T}\partial_x, \tag{B.11}$$

and for $j = 0, 1, \ldots, J$,

$$V_j(x,y) = \frac{\cos(ly + \gamma)\cos(k_j x + \alpha_j)\partial_y\overline{T}}{f\rho H_1}, \tag{B.12}$$

$$\begin{aligned}\psi_j(x,\omega) = {} & \frac{l}{\rho H(A_j^2 + \beta^2 k_j^2)} \\ & \times [\beta k_j \sin(k_j x + \alpha_j) - A_j\cos(k_j x + \alpha_j) \\ & + c_{j1}e^{r_1 x} + c_{j2}e^{r_2 x}],\end{aligned} \tag{B.13}$$

$$\begin{aligned}c_{j1} = {} & (e^{r_2 L_x} - e^{r_1 L_x})^{-1} \\ & \times [\beta k_j \sin(k_j L_x + \alpha_j) - A_j\cos(k_j L_x + \alpha_j) \\ & - (\beta k_j \sin\alpha_j - A_j\cos\alpha_j)e^{r_2 L_x}],\end{aligned} \tag{B.14}$$

$$\begin{aligned}c_{j2} = {} & (e^{r_1 L_x} - e^{r_2 L_x})^{-1} \\ & \times [\beta k_j \sin(k_j L_x + \alpha_j) - A_j\cos(k_j L_x + \alpha_j) \\ & - (\beta k_j \sin\alpha_j - A_j\cos\alpha_j)e^{r_1 L_x}],\end{aligned} \tag{B.15}$$

$$r_{1,2} = \frac{-\beta \pm \sqrt{\beta^2 + 4(-i\omega + \epsilon_c)[-i\omega(l^2 + \lambda^{-2}) + \epsilon_c l^2]}}{2(-i\omega + \epsilon_c)}. \tag{B.16}$$

In (B.14) and (B.15), L_x is the width of the ocean basin.

REFERENCES

Alexander, M. A., 1992a: Midlatitude atmosphere–ocean interaction during El Niño. Part I: The North Pacific. *J. Climate,* **5,** 944–958.

——, 1992b: Midlatitude atmosphere–ocean interaction during El Niño. Part II: The Northern Hemisphere atmosphere. *J. Climate,* **5,** 959–972.

——, and C. Penland, 1996: Variability in a mixed layer ocean model driven by stochastic atmospheric forcing. *J. Climate,* **9,** 2424–2442.

Barnett, T. P., and R. Preisendorfer, 1987: Origins and levels of monthly forecast skill for United States surface air temperatures determined by canonical correlation analysis. *Mon. Wea. Rev.,* **115,** 1825–1850.

Battisti, D. S., U. S. Bhatt, and M. A. Alexander, 1995: A modeling study of the interannual variability in the North Atlantic ocean. *J. Climate,* **8,** 3067–3083.

Bjerknes, J., 1962: Synoptic survey of the interaction between sea and atmosphere in the North Atlantic. *Geofys. Publ.,* **24,** 116–145.

——, 1964: Atlantic air–sea interaction. *Advances in Geophysics,* Vol. 10, Academic Press, 1–82.

Bretherton, C. S., C. Smith, and J. M. Wallace, 1992: An intercomparison of methods for finding coupled patterns in climate data. *J. Climate,* **5,** 541–560.

Cayan, D. R., 1992a: Latent and sensible heat flux anomalies over the northern oceans: Driving the sea surface temperature. *J. Phys. Oceanogr.,* **22,** 859–881.

——, 1992b: Latent and sensible heat flux anomalies over the northern oceans: The connection to monthly atmospheric circulation. *J. Climate,* **5,** 354–369.

Chelton, D. B., and M. G. Schlax, 1996: Global observation of oceanic Rossby waves. *Science,* **272,** 234–238.

Chen, F., and M. Ghil, 1995: Interdecadal variability of the thermohaline circulation and high-latitude surface fluxes. *J. Phys. Oceanogr.,* **25,** 2547–2568.

da Silva, A. M., C. C. Young, and S. Levitus, 1994: Anomalies of heat and momentum fluxes. *Atlas of Surface Marine Data,* Vol. 3, National Oceanic and Atmospheric Administration, 413 pp.

Delworth, T., 1996: North Atlantic interannual variability in a coupled ocean–atmosphere model. *J. Climate,* **9,** 2356–2375.

——, S. Manabe, and R. J. Stouffer, 1993: Interdecadal variations of the thermohaline circulation in a coupled ocean–atmosphere model. *J. Climate,* **6,** 1993–2011.

Deser, C., and M. L. Blackmon, 1993: Surface climate variations over the North Atlantic Ocean during winter: 1900–1989. *J. Climate,* **6,** 1743–1753.

——, and M. S. Timlin, 1997: Atmosphere–ocean interaction on weekly timescales in the North Atlantic and Pacific. *J. Climate,* **10,** 393–408.

Douglas, A. V., D. R. Cayan, and J. Namias, 1982: Large-scale changes in North Pacific and North American weather patterns in recent decades. *Mon. Wea. Rev.,* **110,** 1851–1862.

Ferranti, L., F. Molteni, and T. N. Palmer, 1994: Impact of localized tropical and extratropical SST anomalies in ensembles of seasonal GCM integrations. *Quart. J. Roy. Meteor. Soc.,* **120,** 1613–1645.

Folland, C. K., and D. Parker, 1989: Observed variations of sea surface temperature. *Proc. NATO Advanced Research Workshop on Climate Ocean Interaction,* Kluwer Academic.

Frankignoul, C., 1985: Sea surface temperature anomalies, planetary waves and air–sea feedback in the middle latitude. *Rev. Geophys.,* **23,** 357–390.

——, and K. Hasselmann, 1977: Stochastic climate models, Part II:

Application to sea-surface temperature variability and thermoclime variability. *Tellus,* **29,** 289–305.
——, and P. Müller, 1979: Quasigeostrophic response of an infinite beta-plane ocean to stochastic forcing by the atmosphere. *J. Phys. Oceanogr.*, **9,** 104–127.
——, ——, and E. Zorita, 1997: A simple model of the decadal response of the ocean to stochastic wind forcing. *J. Phys. Oceanogr.,* **27,** 1533–1546.
Gardiner, C. W., 1985: *Handbook of Stochastic Methods for Physics, Chemistry, and the Natural Sciences.* 2d ed. Springer-Verlag, 442 pp.
Ghil, M., and R. Vautard, 1991: Interdecadal oscillations and the warming trend in global temperature time series. *Nature,* **350,** 324–327.
Graham, N. E., 1994: Decadal-scale climate variability in the tropical and North Pacific during the 1970s and 1980s: Observations and model results. *Climate Dyn.,* **10,** 135–162.
——, T. P. Barnett, R. Wilde, M. Ponater, and S. Schubert, 1994: On the roles of tropical and midlatitude SSTs in forcing interannual to interdecadal variability in the winter Northern Hemisphere circulation. *J. Climate,* **7,** 1416–1441.
Grötzner, A., M. Latif, and T. P. Barnett, 1998: A decadal climate cycle in the North Atlantic Ocean as simulated by the ECHO coupled GCM. *J. Climate,* **11,** 831–847.
Gu, D., and S. G. H. Philander, 1997: Interdecadal climate fluctuations that depend on exchanges between the tropics and extratropics. *Science,* **275,** 805–807.
Hall, A., and S. Manabe, 1997: Can local linear stochastic theory explain sea surface temperature and salinity variability? *Climate Dyn.,* **13,** 167–180.
Hasselmann, K., 1976: Stochastic climate models. Part I: Theory. *Tellus,* **28,** 289–305.
Hense, A., R. Glowienka-Hense, H. von Storch, and U. Stähler, 1990: Northern Hemisphere atmospheric response to changes of Atlantic Ocean SST on decadal time scales: A GCM experiment. *Climate Dyn.,* **4,** 157–174.
Horsthemke, W., and R. Lefever, 1984: *Noise-Induced Transitions. Theory and Applications in Physics, Chemistry, and Biology.* Springer-Verlag, 318 pp.
Hurrell, J. W., 1995: Decadal trends in the North Atlantic oscillation: Regional temperatures and precipitation. *Science,* **269,** 676–679.
Jacobs, G. A., H. E. Hurlburt, J. C. Kindle, E. J. Metzger, J. L. Mitchell, W. J. Teague, and A. J. Wallcraft, 1994: Decade-scale trans-Pacific propagation and warming effects of an El Niño anomaly. *Nature,* **370,** 360–363.
Jin, F.-F., 1997: A theory of interdecadal climate variability of the North Pacific ocean–atmosphere system. *J. Climate,* **10,** 324–338.
Kharin, V. V., 1995: The relationship between sea surface temperature anomalies and atmospheric circulation in GCM experiments. *Climate Dyn.,* **11,** 359–375.
Kimoto, M., and M. Ghil, 1993a: Multiple flow regimes in the Northern Hemisphere winter. Part I: Methodology and hemispheric regimes. *J. Atmos. Sci.,* **50,** 2625–2643.
——, and ——, 1993b: Multiple flow regimes in the Northern Hemisphere winter. Part II: Sectorial regimes and preferred transitions. *J. Atmos. Sci.,* **50,** 2645–2673.
Kushnir, Y., 1994: Interdecadal variations in North Atlantic sea surface temperature and associated atmospheric conditions. *J. Climate,* **7,** 141–157.
——, and N. C. Lau, 1992: The general circulation model response to a North Pacific SST anomaly: Dependence on timescale and pattern polarity. *J. Climate,* **5,** 271–283.
——, and I. M. Held, 1996: Equilibrium atmospheric response to North Atlantic SST anomalies. *J. Climate,* **9,** 1208–1220.
Latif, M., and T. P. Barnett, 1994: Causes of decadal climate variability in the North Pacific/North American sector. *Science,* **266,** 634–637.
——, and ——, 1996: Decadal climate variability over the North Pacific and North America: Dynamics and predictability. *J. Climate,* **9,** 2407–2423.
Lau, N. C., 1997: Interactions between global SST and the midlatitude atmospheric circulation. *Bull. Amer. Meteor. Soc.,* **78,** 21–33.
——, and M. J. Nath, 1990: A general circulation model study of the atmospheric response to extratropical SST anomalies observed during 1950–79. *J. Climate,* **3,** 965–989.
——, and ——, 1994: A modeling study of the relative roles of tropical and extratropical SST anomalies in the variability of the global atmosphere–ocean system. *J. Climate,* **7,** 1184–1207.
Lui, Z., 1993: Interannual positive feedback in a simple extratropical air–sea coupling system. *J. Atmos. Sci.,* **50,** 3022–3028.
Luksch, U., 1996: Simulation of North Atlantic low-frequency SST variability. *J. Climate,* **9,** 2083–2092.
——, and H. von Storch, 1992: Modeling the low-frequency sea surface temperature variability in the North Pacific. *J. Climate,* **5,** 893–906.
——, ——, and E. Maier-Reimer, 1990: Modeling North Pacific SST anomalies as a response to anomalous atmospheric forcing. *J. Mar. Syst.,* **1,** 155–168.
Marotzke, J., and J. Willebrand, 1991: Multiple equilibria of the global thermohaline circulation. *J. Phys. Oceanogr.,* **21,** 1372–1385.
Miller, A. J., 1992: Large-scale ocean–atmosphere interactions in a simplified coupled model of the midlatitude wintertime circulation. *J. Atmos. Sci.,* **49,** 273–286.
Münnich, M., M. Latif, S. Venzke, and E. Maier-Reimer, 1998: Decadal oscillations in a simple coupled model. *J. Climate,* **11,** 3309–3319.
Namias, J., 1959: Recent seasonal interactions between North Pacific waters and the overlying atmospheric circulation. *J. Geophys. Res.,* **64,** 631–646.
——, 1963: Large-scale air–sea interactions over the North Pacific from summer 1962 through the subsequent winter. *J. Geophys. Res.,* **68,** 6171–6186.
——, X. Yuan, and D. R. Cayan, 1988: Persistence of atmospheric sea surface temperature and atmospheric flow patterns. *J. Climate,* **1,** 682–703.
Neelin, J. D., and H. A. Dijkstra, 1995: Ocean–atmosphere interaction and the tropical climatology. Part I: The dangers of flux correction. *J. Climate,* **8,** 1325–1342.
Palmer, T. N., and Z. Sun, 1985: A modeling and observational study of the relationship between sea surface temperature in the northwest Atlantic and the atmospheric general circulation. *Quart. J. Roy. Meteor. Soc.,* **111,** 947–975.
Pedlosky, J., 1987: *Geophysical Fluid Dynamics.* 2d ed. Springer-Verlag, 710 pp.
Peng, S., L. A. Mysak, H. Ritchie, J. Derome, and B. Dugas, 1995: The difference between early and middle winter atmospheric response to sea surface temperature anomalies in the northwest Atlantic. *J. Climate,* **8,** 137–157.
——, W. A. Robinson, and M. P. Hoerling, 1997: The modeled atmospheric response to midlatitude SST anomalies and its dependence on background circulation states. *J. Climate,* **10,** 971–987.
Philander, S. G., 1990: *El Niño, La Niña, and the Southern Oscillation.* Academic Press, 293 pp.
Pitcher, E. J., M. L. Blackmon, G. Bates, and S. Muñoz, 1988: The effect of North Pacific sea surface temperature anomalies on the January climate of a general circulation model. *J. Atmos. Sci.,* **45,** 173–188.
Power, S. B., F. Tseitken, M. Dix, R. Kleeman, R. Colman, and D. Holland, 1995: Stochastic variability at the air–sea interface on decadal timescales. *Geophys. Res. Lett.,* **22,** 2593–2596.
Robertson, A. W., 1996: Interdecadal variability over the North Pacific in a multicentury climate simulation. *Climate Dyn.,* **12,** 227–241.
——, and M. Ghil, 1999: Large-scale weather regimes and local climate over the western United States. *J. Climate,* in press.
Saravanan, R., and J. C. McWilliams, 1997: Stochasticity and spatial

resonance in interdecadal climate fluctuations. *J. Climate*, **10,** 2299–2320.

——, and ——, 1998: Advective ocean–atmosphere interaction: An analytical stochastic model with implications for decadal variability. *J. Climate*, **11,** 165–188.

Selten, F. M., R. J. Haarsma, and J. D. Opsteegh, 1999: On the mechanism of North Atlantic decadal variability. *J. Climate*, in press.

Speich, S., H. Dijkstra, and M. Ghil, 1995: Successive bifurcations in a shallow-water model applied to the wind-driven ocean circulation. *Nonlinear Proc. Geophys.*, **2,** 241–268.

Ting, M., and S. Peng, 1995: Dynamics of the early and middle winter atmospheric responses to the Northwest Atlantic SST anomalies. *J. Climate*, **8,** 2239–2254.

Trenberth, K. E., 1990: Recent observed interdecadal climate changes in the Northern Hemisphere. *Bull. Amer. Meteor. Soc.*, **71,** 988–993.

——, and J. Hurrell, 1994: Decadal atmosphere–ocean variations in the Pacific. *Climate Dyn.*, **9,** 303–319.

von Storch, J. S., 1994: Interdecadal variability in a global coupled model. *Tellus*, **46A,** 419–436.

Wallace, J. M., and Q. Jiang, 1987: On the observed structure of the interannual variability of the atmosphere/ocean climate system. *Atmospheric and Oceanic Variability*, H. Cattle, Ed., Royal Meteorological Society, 17–43.

——, C. Smith, and Q. Jiang, 1990: Spatial patterns of atmosphere–ocean interaction in the northern winter. *J. Climate*, **3,** 990–998.

Weare, B., A. Navato, and R. F. Newell, 1976: Empirical orthogonal analysis of Pacific Ocean sea surface temperatures. *J. Phys. Oceanogr.*, **6,** 671–678.

Weaver, A. J., and E. S. Sarachik, 1991: Evidence for decadal variability in an open general circulation model: An advective mechanism. *Atmos.–Ocean*, **29,** 197–231.

——, ——, and J. Marotze, 1991: Freshwater flux forcing of decadal and interdecadal oceanic variability. *Nature*, **353,** 836–838.

Weisse, R., U. Mikolajewicz, and E. Maier-Reimer, 1994: Decadal atmosphere–ocean variations in the Pacific. *J. Geophys. Res.*, **99,** 12 411–12 421.

Weng, W., 1997: A simple model for ocean–atmosphere interaction at midlatitudes. Ph.D. dissertation, University of California, Los Angeles, 128 pp.

——, and J. D. Neelin, 1997: Analytical prototypes for ocean–atmosphere interaction at midlatitudes. Preprints, *Seventh Conf. on Climate Variations*, Long Beach, CA, Amer. Meteor. Soc., 76–78.

——, and ——, 1998: On the role of ocean–atmosphere interaction in midlatitude interdecadal variability. *Geophys. Res. Lett.*, **25,** 167–170.

——, and ——, 1999: Analytical prototypes for ocean–atmospheric interaction at midlatitudes. Part II: Mechanisms for coupled gyre modes. *J. Climate*, in press.

Winton, M., and E. S. Sarachik, 1993: Thermohaline oscillations induced by strong steady salinity forcing of ocean general circulation models. *J. Phys. Oceanogr.*, **23,** 1389–1410.

Yang, J., and J. D. Neelin, 1993: Sea–ice interactions with the thermohaline circulation. *Geophys. Res. Lett.*, **20,** 217–220.

——, and R. X. Huang, 1996: The annual cycle and its role in generating interannual and decadal variations at high latitude oceans. *Geophys. Res. Lett.*, **23,** 269–272.

Yukimoto, S., M. Endoh, Y. Kitamura, A. Kitoh, T. Motoi, A. Noda, and T. Tokioka, 1996: Interannual and interdecadal variabilities in the Pacific in an MRI coupled GCM. *Climate Dyn.*, **12,** 667–683.

Zhang, R.-H., and S. Levitus, 1997: Structure and cycle of decadal variability of upper-ocean temperature in the North Pacific. *J. Climate*, **10,** 710–727.

Zhang, Y., J. M. Wallace, and N. Iwasaka, 1996: Is climate variability over the North Pacific a linear response to ENSO? *J. Climate*, **9,** 1468–1478.

——, ——, and D. S. Battisti, 1997: ENSO-like interdecadal variability: 1900–93. *J. Climate*, **10,** 1004–1020.

Zorita, E., and C. Frankignoul, 1997: Modes of North Atlantic decadal variability in the ECHAM1/LSG coupled ocean–atmosphere general circulation model. *J. Climate*, **10,** 183–200.

——, V. Kharin, and H. von Storch, 1992: The atmospheric circulation and sea surface temperature in the North Atlantic area in winter: Their interaction and relevance for Iberian precipitation. *J. Climate*, **5,** 1097–1108.